

# Formation of Sub-galactic Clouds under UV Background Radiation

Tetsu Kitayama<sup>1,2</sup> and Satoru Ikeuchi<sup>3</sup>

<sup>1</sup> Department of Physics, Tokyo Metropolitan University, Hachioji, Tokyo 192-0397, Japan

<sup>2</sup> Department of Physics, University of Tokyo, Bunkyo-ku, Tokyo 113-0033, Japan

<sup>3</sup> Department of Physics, Nagoya University, Chikusa-ku, Nagoya 464-8602, Japan

e-mail: tkita@phys.metro-u.ac.jp, ikeuchi@a.phys.nagoya-u.ac.jp

## ABSTRACT

The effects of the UV background radiation on the formation of sub-galactic clouds are studied by means of one-dimensional hydrodynamical simulations. The radiative transfer of the ionizing photons due to the absorption by HI, HeI and HeII, neglecting the emission, is explicitly taken into account. We find that the complete suppression of collapse occurs for the clouds with circular velocities typically in the range  $V_c \sim 15 - 40 \text{ km s}^{-1}$  and the 50% reduction in the cooled gas mass with  $V_c \sim 20 - 55 \text{ km s}^{-1}$ . These values depend most sensitively on the collapse epoch of the cloud, the shape of the UV spectrum, and the evolution of the UV intensity. Compared to the optically thin case, previously investigated by Thoul & Weinberg (1996), the absorption of the external UV photon by the intervening medium systematically lowers the above threshold values by  $\Delta V_c \sim 5 \text{ km s}^{-1}$ . Whether the gas can contract or keeps expanding is roughly determined by the balance between the gravitational force and the thermal pressure gradient when it is maximally exposed to the external UV flux. Based on our simulation results, we discuss a number of implications on galaxy formation, cosmic star formation history, and the observations of quasar absorption lines. In Appendix, we derive analytical formulae for the photoionization coefficients and heating rates, which incorporate the frequency/direction-dependent transfer of external photons.

*Subject headings:* cosmology: theory – diffuse radiation – galaxies: formation – radiative transfer

## 1. Introduction

Photoionization of primordial gas is well known to have great impacts on galaxy formation and the thermal history of the universe. The observations of the QSO absorption spectra (Gunn & Peterson 1965) imply that the intergalactic gas has been highly ionized before redshift  $z \sim 5$ . In fact, the existence of an intense ultraviolet (UV) background radiation that can photoionize the universe is inferred from the proximity effect of Ly $\alpha$  forest at  $z = 2 \sim 4$  (e.g. Baljtlík, Duncan & Ostriker 1988; Bechtold 1994; Giallongo et al. 1996). The origin of the UV background radiation could be attributed to the emission from QSO's and/or young galaxies formed at high redshifts (e.g. Couchman 1985; Miralda-Escude & Ostriker 1990; Fukugita & Kawasaki 1994).

The UV background radiation, once produced, largely affects the subsequent formation of structures. In particular, the formation of low-mass objects is suppressed via photoionization and heating associated

with it (Umemura & Ikeuchi 1985; Ikeuchi 1986; Rees 1986; Couchman & Rees 1986; Ikeuchi, Murakami & Rees 1988, 1989; Efstathiou 1992; Babul & Rees 1992; Chiba & Nath 1994; Babul & Ferguson 1996; Okoshi & Ikeuchi 1996; Haiman, Rees, & Loeb 1997; Kepner, Babul & Spergel 1997, among others). Such suppression may partly resolve some of the shortcomings of the hierarchical models of structure formation, such as an excess number of faint galaxies predicted than actually observed (e.g. White & Frenk 1991; Kauffmann, White & Guiderdoni 1993; Cole et al. 1994). In view of this, several authors have simulated the thermal and dynamical evolution of the intergalactic medium under the UV background (Umemura & Ikeuchi 1984; Bond, Szalay & Silk 1988; Murakami & Ikeuchi 1990, 1993; Cen & Ostriker 1992; Zhang, Anninos & Norman 1995; Quinn, Katz & Efstathiou 1996; Thoul & Weinberg 1996; Weinberg, Hernquist & Katz 1997; Navarro & Steinmetz 1997). For instance, Thoul & Weinberg (1996) concluded that the objects with circular velocities  $V_c \lesssim 30 \text{ km s}^{-1}$  are prevented from collapsing at  $2 \lesssim z \lesssim 5$ . These previous studies, however, were based upon the assumption that the medium is optically thin against the ionizing photons. Gas clouds in reality become optically thick in the course of contraction and it is by no means trivial how much the cloud evolution is altered when the radiative transfer of ionizing photons is incorporated. In addition, only the limited range of collapse redshift has been explored previously. As the mean density of the universe depends strongly on redshift in proportion to  $(1+z)^3$ , the effects of the UV background radiation should also vary, with an increasing importance of the radiative transfer at higher redshifts. The possible evolution of the UV background intensity may have further impacts on the cloud dynamics at different redshifts.

In this paper, we study the effects of the UV background radiation on the dynamical evolution of primordial clouds, by means of one-dimensional, spherically symmetric hydrodynamical simulations, incorporating the radiative transfer of the ionizing photons. We use analytical approximations of the photoionization coefficients and heating rates derived in Appendix, which take explicit account of the frequency/direction-dependent radiative transfer due to the absorption by HI, HeI and HeII. They are simply expressed as a function of column densities of each species from the cloud boundary and are applicable to the medium with an arbitrary density profile. By using these analytical formulae, we have achieved a significant reduction of the computational time and are thus able to explore broad ranges in cloud mass scale, collapse redshift, and parameters of the external UV field. The results are compared quantitatively with those of optically thin calculations. Based on the results of numerical simulations, we further predict the global production rate of cooled gas in the standard Cold Dark Matter (CDM) universe and discuss its implications on galaxy formation and cosmic star formation history. We also discuss the imprints of the UV background on the quasar absorption lines, such as the observability of the helium Ly $\alpha$  forests, which can be tested by future observations.

The plan of this paper is as follows. In §2, we describe the numerical model used in this paper. §3 presents the results of our simulation and §4 is devoted to the discussion. Finally §4 summarizes our conclusions. Wherever necessary, the following cosmological parameters are assumed for definiteness; the density parameter  $\Omega_0 = 1$ , the Hubble constant  $h = H_0/(100 \text{ km s}^{-1} \text{ Mpc}^{-1}) = 0.5$ , the baryon density parameter  $\Omega_b = 0.1$ , and the amplitude of the density fluctuations  $\sigma_8 = 0.6$ . The value of  $\sigma_8$  is chosen to match the observed local abundance of galaxy clusters (e.g. Viana & Liddle 1996; Eke, Cole & Frenk 1996; Kitayama & Suto 1997).

## 2. Method

## 2.1. Basic Equations

We simulate the dynamics of a spherically symmetric bound system exposed to the diffuse UV background radiation. The system is a mixture of baryonic gas and collisionless dark matter, with the mass ratio of  $\Omega_b : \Omega_0 - \Omega_b = 1 : 9$ . The evolution of these components is described by the following equations:

$$\frac{dm_b}{dr_b} = 4\pi r_b^2 \rho_b, \quad (1)$$

$$\frac{d^2 r_b}{dt^2} = -4\pi r_b^2 \frac{dP}{dm_b} - \frac{GM(< r_b)}{r_b^2}, \quad (2)$$

$$\frac{du}{dt} = \frac{P}{\rho_b^2} \frac{d\rho_b}{dt} + \frac{\mathcal{H} - \mathcal{L}}{\rho_b}, \quad (3)$$

$$P = (\gamma - 1)\rho_b u = \frac{k_B \rho_b T}{\mu m_p}, \quad (4)$$

and

$$\frac{d^2 r_d}{dt^2} = -\frac{GM(< r_d)}{r_d^2}. \quad (5)$$

Here  $r$ ,  $m$ ,  $\rho$ ,  $P$ ,  $T$ ,  $u$ , and  $\mu$ , are the radius, mass, density, pressure, temperature, internal energy per unit mass, and mean molecular weight in units of the proton mass  $m_p$ , respectively.  $M(< r)$  is the total mass interior to  $r$ ,  $\mathcal{H}$  and  $\mathcal{L}$  are the heating and cooling rates per unit volume,  $G$  is the gravitational constant, and  $k_B$  is the Boltzmann constant. Wherever necessary, the subscripts  $b$  and  $d$  denote baryon and dark matter, respectively. The adiabatic index is fixed at  $\gamma = 5/3$  throughout the paper.

The above equations are solved using the second-order-accurate Lagrangian finite-difference scheme described in Bowers & Wilson (1991) and Thoul & Weinberg (1995). The shocks are treated with the artificial viscosity technique (Richtmyer & Morton 1967; Umemura 1993). The shells are binned equally in mass and their numbers are  $N_b = 500$  for baryonic gas and  $N_d = 5000$  for dark matter. We have performed runs with  $(N_b, N_d) = (2000, 20000)$  and  $(300, 3000)$  and confirmed that our results are robust against the changes in the resolution. We have also checked that our code reproduces accurately the similarity solutions for the adiabatic accretion of collisional gas and for the pressure-less collapse onto a black hole (Bertschinger 1985). The total energy of the system is conserved by better than a few percent in any runs reported in this paper.

## 2.2. Radiative Processes

The baryonic gas is assumed to have the primordial composition with hydrogen and helium mass fractions  $X = 0.76$  and  $Y = 0.24$ , respectively. At each time-step, starting out from the cloud boundary into the interior, we successively solve for the ionization equilibrium among photoionization, collisional ionization and recombination, together with the penetration of the external UV field, as described in detail later in this section. We then compute the heating/cooling rates due to photoionization, collisional ionization/excitation, recombination, thermal bremsstrahlung, and Compton scattering with the cosmic microwave background radiation. Unless otherwise stated, we use the rates and coefficients summarized in Fukugita & Kawasaki (1994), which corrects a few typos in Cen (1992).

The external UV field is taken to be isotropic and have the power-law spectrum:

$$J_{\text{in}}(\nu, z) = J_{21}(z) \left( \frac{\nu}{\nu_{\text{HI}}} \right)^{-\alpha} \times 10^{-21} \text{erg s}^{-1} \text{cm}^{-2} \text{str}^{-1} \text{Hz}^{-1}, \quad (6)$$

where  $J_{21}(z)$  is the intensity (in proper coordinates) at the Lyman limit of hydrogen ( $h\nu_{\text{HI}} = 13.6\text{eV}$ ) and  $\alpha$  is the spectral index. Observations of the proximity effect in the Ly $\alpha$  forest suggest  $J_{21} = 10^{\pm 0.5}$  at  $z = 1.7 - 4.1$  (Baljtlík, Duncan & Ostriker 1988; Giallongo et al. 1996; Cooke, Espey & Carswell 1997; Savaglio et al. 1997), but its value is still highly uncertain at other redshifts. Theoretical predictions of the value of  $J_{21}$  needed to reionize the universe at high redshifts range from  $J_{21} \sim 0.1$  to even  $\sim 100$  (e.g. Fukugita & Kawasaki 1994; Gnedin & Ostriker 1997; Haiman & Loeb 1998; Madau, Haardt & Rees 1999). The predicted epoch at which reionization occurs also has a large uncertainty between  $z \sim 50$  and 6. In the present paper, unless otherwise stated explicitly, we fix the onset of the UV background at  $z_{\text{UV}} = 20$ , and consider the following four cases at  $z < z_{\text{UV}}$ :

1.  $J_{21} = 1$  and  $\alpha = 1$ ,
2.  $J_{21} = 0.1$  and  $\alpha = 1$ ,
3.  $J_{21} = 1$  and  $\alpha = 5$ ,
4. Evolving  $J_{21}$  and  $\alpha = 1$ , where

$$J_{21} = \begin{cases} \left( \frac{1+z}{7} \right)^{-6} & 6 \leq z \leq z_{\text{UV}} \\ 1 & 3 \leq z \leq 6 \\ \left( \frac{1+z}{4} \right)^4 & 0 \leq z \leq 3. \end{cases} \quad (7)$$

The values  $\alpha = 1$  and 5 are chosen to mimic the spectra of quasars and massive stars, respectively. By the above form of the UV evolution (eq.[7]), we attempt to study the effects of a late reionization and a decline of the UV intensity at low redshift.

The incident UV spectrum is modified due to the radiative transfer as it penetrates into the gas cloud. In the present paper, we explicitly take account of the frequency/direction-dependent absorption by HI, HeI, and HeII, using equations (A15) and (A16) in Appendix. Having performed the frequency and angular integrations of the transfer equation neglecting the emission term, the analytical formulae are obtained for the photoionization coefficients and heating rates in the plane-parallel slab. They are simply expressed as a function of column densities of individual species measured from the boundary, and lead to a significant reduction in the computational time. By means of these formulae, we solve simultaneously for the ionization equilibrium in each gas shell and the UV radiation field processed between the outer boundary and that shell. The ionization state of the gas and the radiation field are computed iteratively until the abundances of HI, HeI and HeII all converge to the precision better than 1%.

Note that the above treatment of the radiative transfer systematically overestimates the effect of absorption in the following respects; 1) since the solution of the transfer equation in the plane-parallel geometry is applied to a spherical cloud, the photon path lengths from the outer boundary are overestimated, 2) at each radial point, ionizing photons coming from the inner  $2\pi$  steradian of the cloud is ignored, and 3) the emission (or scatter) of incident photons is neglected. It should thus provide a conservative limit in which an external UV field is maximally weakened and has the minimal effects on cloud evolution. This is in fact complementary to a conventional approximation of the optically thin medium (e.g. Thoul &

Weinberg 1996), in which the external UV field is likely to have the maximal effects on the cloud dynamics. In what follows, therefore, we examine both of these limiting cases and perform quantitative comparisons between them. In so doing, we hope to bracket the true answer, which is still very difficult to solve in a fully self-consistent manner.

The approximation of the ionization equilibrium is correct if the recombination time-scale  $t_{\text{rec}}$  is shorter than the dynamical time-scale  $t_{\text{dyn}} \equiv 1/\sqrt{G\rho}$ . Assuming a high degree of ionization, this yields the following condition for the electron density  $n_e$  (e.g. Vedel, Hellsten & Sommer-Larsen 1994):

$$n_e > 7.1 \times 10^{-6} T_4^{1.4} \left( \frac{2}{1+X} \right) \left( \frac{\Omega_0/\Omega_b}{10} \right) \text{ cm}^{-3}, \quad (8)$$

where  $T_4 \equiv (T/10^4 \text{ K})$ , and we have adopted  $t_{\text{rec}} \equiv (\alpha_{\text{H}} n_e)^{-1}$  using the recombination rate for hydrogen  $\alpha_{\text{H}}$  given in equation (A27). The above condition is satisfied in most situations considered in this paper except at the outer envelopes of clouds at low redshifts. For example, in a cloud collapsing at  $z = 3$ , typically the out-most  $\sim 5\%$  of the gas has the density below the above value at  $z = 3$  (see §2.3 for the definition of the collapse epoch). For these shells, the assumption of the ionization equilibrium will result in overestimating the fractions of neutral species and hence in overestimating the effect of absorption even further. In practice, however, the physical abundances of neutral species in these shells are negligibly small. Thus the approximation of the ionization equilibrium is well justified in the present analysis.

### 2.3. Initial Conditions

We start the simulations when the overdensity of a cloud is still in the linear regime. The initial overdensity profile is assumed to have the form of a single spherical Fourier mode for both baryon and dark matter components:

$$\delta_i(r) = \delta_i(0) \frac{\sin(kr)}{kr}, \quad (9)$$

where  $k$  is the comoving wavenumber, and  $\delta_i(0)$  is the central overdensity. Throughout the paper, we fix  $\delta_i(0) = 0.2$ . Assuming that the initial perturbation is dominated by the growing mode, the initial velocity profile is given by

$$v_i(r) = H_i r \left( 1 - \frac{\bar{\delta}_i(< r)}{3} \right), \quad (10)$$

where  $H_i$  is the Hubble parameter at the initial epoch, and  $\bar{\delta}_i(< r)$  is the volume averaged overdensity within radius  $r$ . The outer boundary is taken at the first minimum of  $\delta_i(r)$ , i.e.  $kr = 4.4934$ , at which  $\bar{\delta}_i(< r)$  vanishes and the shell initially expands at the speed  $H_i r$ . As in Haiman, Thoul & Loeb (1996), we define the baryonic mass enclosed within this radius as the bound mass  $M_{\text{bound}}$ , and that enclosed within the first zero of  $\delta_i(r)$ , i.e.  $kr = \pi$ , as the cloud mass  $M_{\text{cloud}}$ . These masses are related to each other via  $M_{\text{cloud}} = 0.342[1 + 0.304\delta_i(0)]M_{\text{bound}} = 0.363M_{\text{bound}}$ .

Having fixed the initial density profile, we vary the initial redshift  $z_i$  and the cloud mass  $M_{\text{cloud}}$  to simulate different collapse epochs and mass scales, i.e., circular velocities or virial temperatures. We define the central collapse redshift  $z_{c0}$  and the cloud collapse redshift  $z_c$  respectively as the epochs at which the inner-most gas shell and the shell enclosing  $M_{\text{cloud}}$  would collapse to the center in the absence of thermal pressure. The circular velocity  $V_c$  and the virial temperature  $T_{\text{vir}}$  of the cloud are defined using  $M_{\text{cloud}}$  and

$z_c$  as

$$V_c = 15.9 \left( \frac{M_{\text{cloud}} \Omega_0 / \Omega_b}{10^9 h^{-1} M_\odot} \right)^{1/3} (1 + z_c)^{1/2} \text{ km s}^{-1}, \quad (11)$$

$$T_{\text{vir}} = 9.09 \times 10^3 \left( \frac{\mu}{0.59} \right) \left( \frac{M_{\text{cloud}} \Omega_0 / \Omega_b}{10^9 h^{-1} M_\odot} \right)^{2/3} (1 + z_c) \text{ K}. \quad (12)$$

Unless otherwise stated explicitly, we study three combinations of  $z_i$ ,  $z_{c0}$ , and  $z_c$  listed in Table 1. In this table, we also list the turn-around redshifts corresponding to  $z_{c0}$  and  $z_c$ ,  $z_{\text{ta}0} \equiv 2^{2/3}(1 + z_{c0}) - 1$  and  $z_{\text{ta}} \equiv 2^{2/3}(1 + z_c) - 1$ , respectively. In the low-redshift collapse, the gas is exposed to the UV background radiation from the linear regime. In the middle-redshift collapse, the cloud center is close to turn-around at the onset of the UV radiation  $z_{\text{UV}} = 20$ . In the high-redshift collapse, the cloud center has already collapsed prior to  $z_{\text{UV}}$ .

At an initial epoch, the gas is assumed to have the uniform temperature given by

$$T_i = \begin{cases} 2.726(1 + z_i) & \text{if } z_i \geq 200 \\ 548 \left( \frac{1+z_i}{201} \right)^{3(\gamma-1)} & \text{if } z_i < 200, \end{cases} \quad (13)$$

taking account of the fact that the matter is tightly coupled to the cosmic microwave background at  $z \gtrsim 200$  (e.g. Anninos & Norman 1994; Chieze, Teyssier & Alimi 1997).

## 2.4. Boundary Conditions

If the gas is able to lose sufficient energy by radiative cooling, it falls towards the center nearly at the free-fall rate. As the density increases near the center, the cooling time-scale  $t_{\text{cool}} \equiv u\rho/|\mathcal{H} - \mathcal{L}|$  and the dynamical time-scale  $t_{\text{dyn}}$  become extremely small, and infinitely large number of time-steps are required in the simulation. In order to avoid this, we introduce the following criteria. If a gas shell reaches below some minimum radius  $r_{\text{min}}$  and satisfy  $t_{\text{cool}}/t_{\text{dyn}} < 0.01$ , then we regard it as having cooled and collapsed; we move the shell to the center and ignore in the rest of the simulation, except in the calculation of the gravitational force. When dropping a shell to the center, we assume that the next shell expands inward adiabatically to cover the volume of the dropped shell. The evolution of each shell is traced until both of the above criteria are fulfilled. We adopt as  $r_{\text{min}}$  the radius at which the system attains rotational support (e.g. Padmanabham 1993):

$$r_{\text{min}} = 0.05 \left( \frac{\Omega_b / \Omega_0}{0.1} \right)^{-1} \left( \frac{\lambda_{\text{ta}}}{0.05} \right)^2 r_{\text{ta}}, \quad (14)$$

where  $r_{\text{ta}}$  is the turn-around radius of the gas shell, and  $\lambda_{\text{ta}}$  is the dimensionless spin parameter attained by turn-around. We fix  $\lambda_{\text{ta}} = 0.05$  based on the results of the numerical simulations (Efstathiou & Jones 1979; Barns & Efstathiou 1987; Warren et al. 1992). Equation (14) also gives the scale under which the assumption of spherical symmetry breaks down. The baryon mass that has collapsed to the center is denoted by  $M_{\text{coll}}$ .

The dynamical time-scale also becomes very small when collisionless dark matter shells approach the center. We therefore rebound the dark matter shells near the center (Spitzer & Hart 1971; Gott 1975). As noted by Thoul & Weinberg (1995), it is desirable to choose the rebounding radius  $r_{\text{reb}}$  that is small enough not to alter the evolution of gas shells, but not too small to degrade energy conservation. In order

to achieve these, we set  $r_{\text{reb}}$  equal to  $r_{\text{min}}$  of a gas shell that encloses  $0.01 - 0.1M_{\text{bound}}$  depending on a run. Throughout each run,  $r_{\text{reb}}$  is fixed at this value.

At the outer boundary, we adopt the free boundary condition, i.e. the pressure outside the cloud  $P_{\text{out}}$  is zero. We have also performed runs with a mirror boundary condition ( $P_{\text{out}} = P_{N_b}$ , where  $P_{N_b}$  is the pressure of the outermost gas shell) and confirmed that our results remain essentially invariant.

### 3. Numerical Results

#### 3.1. Dynamical evolution

Figure 1 illustrates the trajectories of gas shell radii in the low-redshift collapse ( $z_c = 0.5$ ) for a cloud with  $V_c = 32 \text{ km s}^{-1}$  ( $M_{\text{cloud}} \simeq 9 \times 10^8 M_{\odot}$ ). In the absence of the UV background, the gas shells initially comoving with the Hubble expansion will eventually turn around due to gravity and start to contract. As the virial temperature of the cloud is  $T_{\text{vir}} \simeq 4 \times 10^4 \text{ K}$ , the gas can lose energy efficiently by radiative cooling and collapse towards the center. If the UV background radiation is present, on the contrary, the evolution of the cloud is significantly altered. Figure 1 (a) shows that the cloud is prohibited to collapse completely under a constant UV with  $J_{21} = 1$  and  $\alpha = 1$ . Once, however, the UV amplitude is reduced to  $J_{21} = 0.1$  and the absorption is taken into account, the inner part of the cloud may start to collapse (Fig. 1b). Alternatively, a softer spectrum  $\alpha = 5$  enables larger number of shells to collapse by  $z = 0$  (Fig. 1c). The cloud collapse is also promoted if the UV background radiation evolves according to equation (7) (Fig. 1d).

In order to study the above mentioned features in more detail, we plot in Figure 2 the evolution of the temperature  $T$ , HI fraction  $X_{\text{HI}} \equiv n_{\text{HI}}/(n_{\text{HI}} + n_{\text{HII}})$ , HI column density measured from the outer boundary  $N_{\text{HI}}$ , and HeII fraction  $X_{\text{HeII}} \equiv n_{\text{HeII}}/(n_{\text{HeI}} + n_{\text{HeII}} + n_{\text{HeIII}})$  in the runs shown in Figure 1. For  $J_{21} = 1$  and  $\alpha = 1$ , temperature rises to  $T \sim 10^4 \text{ K}$  and all the gas is photoionized almost instantaneously at the onset of the UV background  $z_{\text{UV}} = 20$  (Fig. 2a). At this epoch, the cloud density is still almost equal to the mean of the universe ( $n_{\text{H}} \sim 2 \times 10^{-3} \text{ cm}^{-3}$ ) and the external UV field can penetrate into the cloud center, even if the absorption is considered. The thermal pressure of the heated gas takes over the gravity and the cloud keeps expanding.

For a smaller UV amplitude  $J_{21} = 0.1$ , Figure 2(b) shows that the cloud evolves very differently with/without the absorption. If the absorption is considered, the central part of the cloud is not ionized instantaneously, but stays neutral until the gas density decreases significantly due to expansion. It is noticeable that the temperature still rises almost instantaneously to  $T \sim 10^4 \text{ K}$ . This is because the time-scale for heating is much shorter than that for ionization (e.g. Gnedin & Ostriker 1997). One can roughly estimate the ratio of these time-scales in the case of  $\alpha = 1$  as

$$\begin{aligned} \frac{t_{\text{heat}}}{t_{\text{ion}}} &= \frac{3k_{\text{B}}T}{2\mathcal{H}_{\text{HI}}} \Gamma_{\text{HI}}^{-1} \\ &= \begin{cases} 0.285T_4 & \text{optically thin limit,} \\ 7.28 \times 10^{-2}T_4\tau_{\text{HI}}^{-1/3} & \text{optically thick limit,} \end{cases} \end{aligned} \quad (15)$$

where  $\tau_{\text{HI}} = 6.3 \times 10^{-18}(N_{\text{HI}}/\text{cm}^{-2})$  is the HI optical depth at the Lyman limit  $\nu_{\text{HI}}$ , and  $\Gamma_{\text{HI}}$  and  $\mathcal{H}_{\text{HI}}$  are photoionization coefficient and heating rate derived for the pure hydrogen gas in Appendix (eqs [A22]–[A25]). At  $z_{\text{UV}}$ , the HI column density at the center is  $N_{\text{HI}} \sim 10^{20} \text{ cm}^{-2}$  in Figure 2(b), which gives the optical depth of  $\tau_{\text{HI}} = 630$  and  $t_{\text{heat}}/t_{\text{ion}} = 8.5 \times 10^{-3}T_4$  in the above equation. For a softer

spectrum, this ratio becomes larger and the heating becomes relatively slower as illustrated in Figure 2(c). In this case, the pressure gradient between the cold neutral center of the cloud and the hot ionized envelope causes to push the gas slightly inward near the cloud center at  $z \sim 10$  (Fig. 1 c).

Figure 2(b) further indicates that as the gravity overcomes the pressure support, the gas shells can turn around and the density starts to rise again. The gas is first heated by shock and adiabatic compression, but it will start to lose energy and shrink to the center once the radiative cooling becomes efficient. Consequently the neutral core is formed at the center. The absorption of the external UV field promotes the cloud collapse and the formation of the neutral core, by both reducing the number of photoionized ions and lowering the heating rate.

The cloud evolution is very sensitive to the spectral index of the UV background. For a softer spectrum  $\alpha = 5$ , there are smaller numbers of high energy photons, and hence larger numbers of HeII, than for  $\alpha = 1$  (Fig. 2c). The larger number of shells are thus able to collapse within a given time for  $\alpha = 5$ .

If the UV background evolves according to equation (7), the gas in the cloud is ionized gradually as in Figure 2(d). As the UV intensity drops at  $z < 3$ , the neutral fraction starts to rise again and the inner shells start to collapse to the center.

Figure 3 shows the radial profiles at  $z = 0$  in some of the runs discussed above. The shock front (if exists) is at  $r \sim 10^2$  kpc. The density profile inside the shock front agrees well with the self-similar solution  $\rho \propto r^{-2.25}$  (Bertschinger 1985). The central part of the cloud is self-shielded against the external UV photons and the gas becomes neutral. In the case of  $(J_{21}, \alpha) = (0.1, 1)$  with absorption, the simulated profiles of  $X_{\text{HI}}$  and  $N_{\text{HI}}$  roughly agree with an analytical estimation for the pure hydrogen gas presented in Appendix. For instance, inserting into equation (A29) the values read off from the figure at  $r \sim 2$  kpc, ( $n_{\text{H}} \sim 10^{-2} \text{cm}^{-2}$ ,  $T \sim 10^4 \text{K}$ , and  $X_{\text{HI}} \sim 0.1$ ), we obtain  $\tau_{\text{HI}} \sim 2$ , i.e.  $N_{\text{HI}} \sim 3 \times 10^{17} \text{cm}^{-2}$ , in good accordance with Figure 3(c). On the contrary, such an estimation breaks down for the softer spectrum ( $\alpha = 5$ ) because of the larger abundances of HeI and HeII.

The effects of the UV background radiation become less significant as the cloud mass increases. Figure 4(a) shows that the gas collapse is still delayed by the UV radiation for a cloud with  $V_c = 50 \text{ km s}^{-1}$  ( $M_{\text{cloud}} \simeq 3 \times 10^9 M_{\odot}$ ,  $T_{\text{vir}} \simeq 9 \times 10^4 \text{ K}$ ). The evolution, however, is only slightly altered for a larger cloud with  $V_c = 100 \text{ km s}^{-1}$  ( $M_{\text{cloud}} \simeq 3 \times 10^{10} M_{\odot}$ ,  $T_{\text{vir}} \simeq 4 \times 10^5 \text{ K}$ ). The effects of absorption, compared to the optically thin case, also become insignificant at this mass scale as the collisional ionization dominates the photoionization.

Figures 5 and 6 illustrate the trajectories of gas shells in the middle-redshift collapse ( $z_c = 3$ ). Since the density of a cloud is higher than the low-redshift collapses discussed above, the larger amount of gas is able to collapse for a given circular velocity  $V_c = 32 \text{ km s}^{-1}$ . At the onset of the UV background  $z_{\text{UV}} = 20$ , the cloud center is about to turn around, and the density is  $n_{\text{H}} \sim 10^{-2} \text{ cm}^{-3}$ , roughly a factor of 5 larger than the mean density of the Universe. At this density, the inner part of the cloud can be kept self-shielded against ionizing photons until it collapses if the absorption is considered (Fig. 6b,c,d). Even in such cases, the gas is still heated promptly to  $T \sim 10^4 \text{K}$  for  $\alpha = 1$ , because of the high efficiency of heating process over ionization mentioned above (eq. [15]).

The effects of the UV background radiation is further weakened if one goes to even higher redshifts. Figure 7 shows the gas shell trajectories in the high-redshift collapse ( $z_c = 10$ ). At  $z_{\text{UV}}$ , about 10% of  $M_{\text{bound}}$  have already collapsed, and a number of shells either have turned around or are about to turn around. In addition, Compton cooling further promotes the gas collapse at  $z \gtrsim 7$ .



### 3.2. Critical mass-scales for the collapse

In order to quantify the results presented in §3.1, we plot in Figure 8 the fraction of gas mass which has cooled and collapsed to the center after the UV onset  $z_{\text{UV}} = 20$  as a function of circular velocity. The output epochs correspond to  $t = 0.5t_c, t_c, 2t_c$ , where  $t_c = t_0/(1 + z_c)^{3/2}$  and  $t_0$  is the present age of the universe. In the low and middle redshift collapses ( $z_c = 0.5$  and  $3$ ), there exists a sharp cut-off in the collapsed fraction and this threshold lies in the range  $V_c = 20 \sim 50 \text{ km s}^{-1}$  depending on different assumptions on the UV background. In the high-redshift collapse ( $z_c = 10$ ), on the contrary, the threshold is not so distinct and smaller cloud is able to collapse against the external UV.

We define the cut-off velocity  $V_c^{\text{cut}}$  and the half-reduction velocity  $V_c^{\text{half}}$ , respectively, as the velocities at which the mass collapsed between  $z_{\text{UV}}$  and  $z_c$  is 0.05 and 0.5 of that with no UV. Figure 9 illustrates that these quantities depend most largely on the UV spectral index  $\alpha$ , the evolution of the UV flux, and the collapsing redshift  $z_c$  (we have added to this figure the results for the runs with  $z_c = 0, 1.4, 4.8$  and  $6.2$ ). Compared to the optically thin cases, the adoption of the radiative transfer systematically lowers  $V_c^{\text{cut}}$  and  $V_c^{\text{half}}$  by about  $5 \text{ km s}^{-1}$ .

For a constant UV flux (Figs 9 a–c), both  $V_c^{\text{cut}}$  and  $V_c^{\text{half}}$  decrease with increasing  $z_c$ , because of higher gas density and stronger Compton cooling. At  $z_c \gtrsim 7$ , the central part of the cloud begins to collapse prior to  $z_{\text{UV}}$  and  $V_c^{\text{cut}}$  falls below  $15 \text{ km s}^{-1}$ , corresponding to  $T_{\text{vir}} \sim 8000\text{K}$  (note that  $V_c^{\text{cut}}$  and  $V_c^{\text{half}}$  are evaluated from the amount of gas cooled after the UV onset). We simply omit the data points from the figures at such low velocities, since it is beyond the scope of our current framework to study these regimes where the molecular cooling dominates.

In the presence of the UV evolution (Fig. 9d),  $V_c^{\text{cut}}$  and  $V_c^{\text{half}}$  rise rapidly with time at high redshifts and then begin to drop at low redshifts. However, the peaks of these quantities are at  $z_c \sim 1.5$ , which is much later than the peak of the UV flux ( $z = 3 - 6$ ). This is because the kinetic energy of expanding gas particles delays the cloud collapse significantly even after the UV flux starts to decline. The late infall of gas after the decline of the UV background is therefore suppressed until  $z_c \lesssim 1$ .

So far we have fixed the onset of the UV background at  $z_{\text{UV}} = 20$ . This choice is rather arbitrary given the large uncertainties in the reionization history of the universe. A possibility of much later reionization (smaller  $z_{\text{UV}}$ ) can be covered effectively by the UV evolution of the form (7). In order to examine an alternative possibility of much earlier reionization, we performed a few runs with  $z_{\text{UV}} = 50$  and added the resultant  $V_c^{\text{cut}}$  to Figure 9(a). The differences from the fiducial  $z_{\text{UV}} = 20$  runs are significant only for the high-redshift collapse ( $z_c = 10$ ), because the gas shells infalling at  $z = 20 - 50$  are mainly affected. At such high redshifts, the effect of the radiative transfer of UV photons becomes large because the cloud density is very high.

Figure 10 shows the baryon mass  $M^{\text{half}}$  corresponding to  $V_c^{\text{half}}$  as a function of  $z_c$ . Also plotted for reference are the Jeans mass with  $T = 10^4\text{K}$  and the masses corresponding to  $1, 2, 3\sigma$  density perturbations in the standard CDM universe with  $\Omega_0 = 1$ ,  $h = 0.5$ ,  $\Omega_b = 0.1$ , and  $\sigma_8 = 0.6$ . The cloud well above  $T_{\text{vir}} = 10^4\text{K}$  is significantly affected by the UV background radiation. For a constant UV flux,  $M_b^{\text{half}}$  rises at a rate faster than  $(1 + z_c)^{-3/2}$ , which is expected for the Jeans mass with constant temperature. This is because  $V_c^{\text{half}}$  increases with decreasing  $z_c$  as shown in Figures 9 (a)–(c). For the evolving UV,  $M_b^{\text{half}}$  keeps growing even after the decline of the UV background and the growth slows down considerably only at  $z \lesssim 1$ .

Figure 10 further indicates that the collapse of  $\lesssim 2\sigma$  density fluctuations in the standard CDM universe is highly suppressed at low masses by the UV background radiation. For example, the cooled mass

from a  $1\sigma$  fluctuation is reduced to less than 50% at  $M_{\text{cloud}} \lesssim 10^9 M_{\odot}$  and  $z_c \gtrsim 2$  for  $(J_{21}, \alpha) = (1, 1)$ , and at  $M_{\text{cloud}} \lesssim 2 \times 10^8 M_{\odot}$  and  $z_c \gtrsim 3$  for  $(J_{21}, \alpha) = (1, 5)$  (see also §4.2 for more discussion on the implications on structure formation).

## 4. Discussion

### 4.1. Comparison with analytical estimates

The results of our simulations are compared with analytical estimates on the density–temperature diagrams (e.g. Efstathiou 1992; Chiba & Nath 1994) in Figure 11. We divide the simulation results into three categories and denote their virial density  $n_{\text{H}}^{\text{vir}} = 3.80 \times 10^{-5} (\Omega_b h^2 / 0.025) (X/0.76) (1 + z_c)^3 \text{ cm}^{-3}$  and the virial temperature  $T_{\text{vir}}$  by different symbols; 1) *efficient cooling* (circles), if the gas mass  $M_{\text{cloud}}$  can cool before  $t_c + t_{\text{dyn}}$ , 2) *moderate cooling* (triangles), if  $M_{\text{cloud}}$  can cool only within the present age of the universe  $t_0$ , and 3) *inefficient cooling* (crosses), if otherwise. For comparison, three analytical relations are computed, using the same UV parameters as the simulations except for assuming optically thin in all cases;  $t_{\text{cool}} = t_{\text{dyn}}$  (solid line),  $t_{\text{cool}} = t_0 - t_c$  (dashed), and  $T_{\text{vir}} = T_{\text{eq}}$  (dotted), where  $T_{\text{eq}}$  is the temperature at which the cooling and heating rates balance ( $\mathcal{H} = \mathcal{L}$ ). The former two analytical relations are evaluated using  $n_{\text{H}}^{\text{vir}}$  at  $z_c$ , while the last one using  $n_{\text{H}}^{\text{ta}} = n_{\text{H}}^{\text{vir}}/8$  at the turn-around epoch  $z_{\text{ta}}$ .

Figure 11 shows that our simulation results under a constant UV are in reasonable agreement with the analytic estimates defined above; 1) *efficient cooling* lies in the region where  $t_{\text{cool}} < t_{\text{dyn}}$ ,  $t_{\text{cool}} < t_0 - t_c$  and  $T_{\text{vir}} > T_{\text{eq}}$ , 2) *moderate cooling* mainly lies where  $t_{\text{dyn}} < t_{\text{cool}} < t_0 - t_c$  and  $T_{\text{vir}} > T_{\text{eq}}$ , 3) *inefficient cooling* lies where  $t_{\text{cool}} > t_0 - t_c$  or  $T_{\text{vir}} < T_{\text{eq}}$ . Such correspondences degrade near the boundaries of each region. Compared to the optically thin runs, cooling efficiency is systematically enhanced to some extent if the absorption is taken into account.

It should be noted that, in order to achieve above agreements, it is essential to evaluate the relation  $T_{\text{vir}} = T_{\text{eq}}$  at  $z_{\text{ta}}$ , not at  $z_c$  (if evaluated at  $z_c$ , the dotted lines in Fig. 11 are shifted downwards by a factor of 8). This is because the cloud evolution largely depends on the photoionization prior to the collapse. Roughly speaking, whether the gas can contract or keeps expanding is determined by the balance between the gravitational force and the thermal pressure gradient when it is “maximally exposed” to the external UV flux, i.e., when the gas attains the maximum value of  $J_{21}/n_{\text{H}}$ . For the gas exposed to the constant UV flux from the linear regime, this corresponds to the turn around. The above statement also applies in the presence of the evolution in the UV intensity.

### 4.2. Cosmological implications

The suppression of low-mass objects by the UV background radiation has profound implications on cosmology and galaxy formation. Given the fraction of cooled gas in objects of different masses and collapse redshifts from the simulations, we can deduce the abundance distribution of collapsing objects in the entire Universe. Specifically, we compute the baryon mass density that cools and collapses per unit redshift as a function of the collapsed mass  $M_{\text{coll}}$  of baryons in a halo and the collapse epoch  $z_c$  as

$$\frac{d^2 \rho_{\text{coll}}(M_{\text{coll}}, z_c)}{dM dz} = M_{\text{coll}} \frac{d^2 N_{\text{halo}}^{\text{f}}(M_{\text{coll}} \Omega_0 / f_{\text{coll}} \Omega_b, z_c)}{dM dz}, \quad (16)$$

where  $f_{\text{coll}}$  is the collapse fraction of a cloud relative to the pressure-less case, and  $d^2 N_{\text{halo}}^f(M, z)/dMdz$  is the comoving number density of halos with mass  $M$  that collapse and form per unit redshift at  $z$ . We use the latter quantity rather than a conventional mass function, e.g. that of Press & Schechter (1974), because  $f_{\text{coll}}$  obtained in our simulations is more closely related to clouds just collapsing at a given redshift. Unfortunately, there is not yet a fully self-consistent analytical formalism to compute this quantity, while several approaches have been proposed (e.g. Bond et al. 1991; Lacey & Cole 1993; Sasaki 1994; Kitayama & Suto 1996a,b; Manrique & Salvador-Sole 1996). In this paper, as a working hypothesis, we adopt the halo formation rate given by equation (15) of Kitayama & Suto (1996a) with the threshold mass  $M_f = M/2$  (see their paper for detail). We have checked that our results are qualitatively unchanged by adopting an alternative approach by Sasaki (1994).

Figure 12 illustrates the baryon mass distribution of collapsing objects in the standard CDM universe. In the absence of pressure, collapsing objects have a broad mass distribution with an increasing fraction of high mass objects at lower redshifts. Once the gas pressure is taken into account, high mass objects are reduced by the low cooling efficiency, and low mass objects by the UV background. As a result, the abundance distribution at  $z_c \lesssim 3$  agrees well with the observed mass range of galaxies. Note that the low mass end of the distribution has a tail, not a sharp cut-off. This is because the objects just above  $V_c^{\text{cut}}$  can have a wide range of  $M_{\text{coll}}$  for almost identical  $M_{\text{cloud}}$ . Thus the collapse of dwarf-sized objects of mass  $M_{\text{coll}} \lesssim 10^9 M_\odot$  is still possible at  $z_c \sim 0.5$ , but such objects are expected to have lower baryon fraction than normal galaxies. This point can be tested by future observations.

One can integrate the above distribution over mass to obtain the total amount of baryon that is collapsing at a given epoch. Figure 13 shows the evolution of this quantity (denoted by “cold gas + star”). We have also deduced similarly from our simulations the baryon mass density that becomes bound by the gravity of clouds but not yet cooled at  $z_c$ . Such a component, denoted by “hot gas”, is mainly contained in objects corresponding to groups and clusters of galaxies. We further define “unbound gas” as the gas that becomes unbound due to the UV background but would have collapsed at  $z_c$  in the absence of pressure. Figure 13 indicates that the production rate (per Hubble time at a given epoch) of “cold gas + star” has a peak at  $z_c \sim 2 - 3$  and it is rather insensitive to the UV parameters. This seems to suggest a high efficiency of star formation activity at these redshifts. On the other hand, the production rate of “hot gas” and that of “unbound gas” simply increases and decreases with time, respectively (see also Barkana & Loeb 1999; Cen & Ostriker 1999).

Figure 14 further compares the predicted production rate (per year) of “cold gas + star” in the standard CDM universe with the observed cosmic star formation rate (SFR, Madau et al. 1996, 1998; Lilly et al. 1996; Connolly et al. 1997) compiled by Totani et al. (1997) and Totani (1999, private communication). This comparison is only demonstrative, since the predicted curves simply set an upper limit to the global SFR in the universe and their normalization can be shifted in proportion to the baryon density parameter  $\Omega_b$ . Nonetheless, it is noticeable that the predicted production rates of “cold gas + star” under the UV background show a steep rise at  $z \lesssim 1$ , in good qualitative accordance with what is actually seen in the SFR data. At higher redshifts, they continue to rise up to  $z \sim 4$  and then flatten. This is somewhat different from a rather sharp decline at  $z \sim 2 - 4$  in the observed SFR. It should be kept in mind, however, that these SFR data are still very uncertain due to the dust extinction and may be shifted upward by large factors (e.g. Pettini et al. 1998). Recent detections of star forming galaxies in the submm band also suggest rather high SFR of  $\gtrsim 2 \times 10^{-1} h M_\odot \text{yr}^{-1} \text{Mpc}^{-3}$  at  $z \sim 2 - 4$  (Smail, Ivison & Blain 1997; Hughes et al 1998; Berger et al. 1998). More detailed discussion on this subject should await higher precision data from future infrared observations.

### 4.3. Imprints on quasar absorption lines

The effects of the UV background radiation on the intergalactic medium can be observed most directly by means of absorption lines of quasar spectra. In order to discuss the impacts of current results on such observations, we plot in Figure 15 the line of sight column densities through the cloud  $N_j^p$  ( $j = \text{HI}, \text{HeI}, \text{HeII}$ ) as a function of impact parameter  $p$ . Here, we restrict the observability of these elements to the column densities  $N_j^p > 10^{14} \text{cm}^{-2}$ , and define the critical impact parameter  $p_{\text{crt}}$  within which the column density is greater than  $10^{14} \text{cm}^{-2}$ . As the column density of each element is too small to be detected except at the central region in the case of  $J_{21} = 1$  and  $\alpha = 1$ , we focus on the other two cases of UV parameters shown in Figure 15. In Tables 2 and 3, we summarize  $p_{\text{crt}}$  and the ratio of its square value, which corresponds to the ratio of area, i.e., the relative expected number. These tables suggest that a large number of helium forest lines are expected especially under the soft UV spectrum. Recent observations by HST in fact indicate the detections of numerous HeII lines (Hogan, Anderson & Rugers 1997; Reimers et al. 1997; Anderson et al. 1999).

If we fit the lines in Figure 15 at  $N_j^p > 10^{14} \text{cm}^{-2}$  by a single power-law  $N_j^p \propto p^{-n}$ , then the column density distribution of each absorption line is written as  $dN/dN_j^p \propto (N_j^p)^{-\beta}$  with  $\beta = (n + 2)/n$ . In Table 4, we summarize  $n$  and  $\beta$  values. Since these are crude numbers, we merely present the values in the case of evolving  $J_{21}$  at  $z_c = 0.5$  and ignore the dependence on redshift and UV parameters. At  $N_{\text{HI}}^p > 10^{16} \text{cm}^{-2}$ , the column density distribution of HeI is similar to that of HI while that of HeII is a little steeper. These points can be checked by future observations.

The above results are also clearly seen in Figure 16, which plots the line of sight column densities of HeI and HeII against the HI column density. The relations among these column densities are rather insensitive to  $V_c$  and  $z_c$ , and are summarized in Table 5 (values are given for  $V_c = 32 \text{ km s}^{-1}$  and  $z_c = 0.5$ ). In order for the HeI lines to be detected at  $N_{\text{HeI}}^p > 10^{14} \text{cm}^{-2}$ , the corresponding HI forest lines are required to have  $N_{\text{HI}}^p > 10^{14} - 10^{16} \text{cm}^{-2}$ . On the other hand, HeII forest lines are more easily detectable and are even saturated at  $N_{\text{HI}}^p > 10^{16} \text{cm}^{-2}$ .

In addition to the high observability of the helium absorption lines at the UV wavelengths, our results further suggest an interesting feature in the HI absorption lines at high column densities. When the line of sight passes near the central region of a cloud that has just collapsed, the gas is expected to be neutral but the temperature can be as high as  $10^4 \text{K}$ , because the time-scale of ionization is longer than that of the photoionization heating (eq. [15]). It should be kept in mind that if the hydrogen molecules, ignored in the present paper, are present, they could allow cooling below  $10^4 \text{K}$ . In any case, the existence of the warm neutral gas could be checked by the HI absorption lines with a large Doppler parameter and the 21cm emission line with high spin temperature. Incidentally the recent observations of damped Ly $\alpha$  systems (Lane et al. 1998; Chengalur & Kanekar 1999) suggest the detection of neutral gas with the spin temperature  $\sim 10^3 \text{K}$ , which is much higher than what is found in normal spiral galaxies.

## 5. Conclusions

We have shown that the formation of the sub-galactic clouds is greatly prevented by the UV background radiation even if the transfer of the external UV photon is taken into account. Within the range of parameters investigated in this paper ( $J_{21} \leq 1$ ,  $\alpha = 1, 5$ ,  $z_c = 0 - 10$ ), the complete suppression of collapse occurs for the clouds with circular velocities typically in the range  $V_c \sim 15 - 40 \text{ km s}^{-1}$  and the 50% reduction in the cooled gas mass with  $V_c \sim 20 - 55 \text{ km s}^{-1}$ . These values depend most sensitively on

the collapse redshift  $z_c$  and the slope of the UV spectrum  $\alpha$ .

The evolution of the UV background also affects the above thresholds in a significant manner. The decline of the UV intensity at  $z \lesssim 3$  can decrease the threshold circular velocities at lower redshifts. This effect, however, is delayed until  $z \lesssim 1.5$  due to the kinetic energy of gas particles attained at higher redshifts. In fact, whether the gas can contract or keeps expanding is roughly determined by the balance between the gravitational force and the thermal pressure gradient when the gas attains the maximum value of  $J_{21}/n_{\text{H}}$ .

As far as the evolution of the gas down to  $T \sim 10^4\text{K}$  is considered, the radiative transfer of the ionizing photons has the moderate effect. Compared to the optically thin case, the absorption of the UV photons by the intervening medium systematically lowers the above threshold values by  $\Delta V_c \sim 5 \text{ km s}^{-1}$ . Once the evolution below  $T \sim 10^4\text{K}$  is taken into account, incorporating the formation and destruction of hydrogen molecules, the radiative transfer is expected to be of greater significance (Haiman, Rees & Loeb 1996, 1997). We will investigate the dynamical evolution of the gas clouds in this regime in future publications (Kitayama et al. in preparation; see also Susa & Umemura 1999).

Our calculations are in good accordance with those of Thoul & Weinberg (1996), for the the same set of parameters, i.e. in the optically thin case and  $z_c = 2 - 5$ . This gives an important cross-check of the current results and confirms that they are insensitive to the different choices of initial conditions and central boundary conditions between their calculations and ours (see §2.4 and §4.1 of Thoul & Weinberg 1995).

Based on the results of numerical simulations, we have predicted the global production rates of cold gas, hot gas, and unbound gas in the standard CDM universe. The abundance distribution of the cold gas matches well the observed mass ranges of dwarfs and galaxies. The global production rate of cooled gas is found to rise steeply from the local universe to  $z \sim 2 - 3$ , indicating a higher efficiency of star formation activity at high redshifts.

We further predict that a large number of the HeII and HeI forest lines may arise in the quasar spectra at the UV wavelengths, which can be detected by HST and future space missions. Such observations should provide powerful probes of the physical state of the intergalactic medium, such as the gas kinematics, and the UV background spectrum (e.g. Sargent et al. 1980; Rauch 1998). In addition, the existence of the warm neutral gas is inferred, due to the high efficiency of heating over ionization. The temperature of such gas can be as high as  $\sim 10^4\text{K}$  and it may be related to the high spin temperatures suggested from the 21cm absorption line observations in the nearby damped Ly $\alpha$  systems (Lane et al. 1998; Chengalur & Kanekar 1999). In testing these predictions, it is essential to perform the multi-line analyses of the absorption systems, which will become possible with greater precisions in near future.

We thank Naoteru Gouda, Izumi Murakami, Tatsushi Sugihara, Hajime Susa, Yasushi Suto and Masayuki Umemura for discussions, and the referee, Rennan Barkana, for helpful comments on the manuscript. We are also grateful to Masahiro Kawasaki and Hideyuki Suzuki for suggestions on the numerical code, and Tomonori Totani for providing the SFR data. T.K. acknowledges a fellowship from Japan Society for the Promotion of Science.

## A. An analytical solution for radiative transfer: photoionization coefficients and heating rates of primordial gas

We derive analytical formulae for the photoionization coefficients and heating rates of a radiation field penetrating into primordial gas aligned in a plane parallel geometry, with an arbitrary density profile. The frequency/direction-dependent radiative transfer due to the absorption by multiple species is explicitly taken into account. While the gas composed of atomic hydrogen and helium is considered here, the formalism can be readily extended to include other species. The derived formulae are applicable to a variety of problems, e.g., the reionization of the universe, and the photoionization of a mini-pancake or low-metallicity gas in galactic haloes.

### A.1. Derivation

Suppose that an isotropic incident radiation field is processed through a gas slab composed mainly of atomic hydrogen and helium. For simplicity, we neglect the emission and scattering of photons by the intervening medium and only consider the absorption above the ionization energy of each species. We model the incident radiation spectrum as a power law with an index  $\alpha$ :

$$I_0(\nu) = I_0(\nu_{\text{HI}}) \left( \frac{\nu}{\nu_{\text{HI}}} \right)^{-\alpha}, \quad (\text{A1})$$

where  $I_0(\nu_{\text{HI}})$  is the specific intensity at the ionization frequency of neutral hydrogen  $\nu_{\text{HI}}$ . Then the processed mean intensity at an arbitrary point inside the slab is written as

$$J(\nu) = \frac{1}{4\pi} \int d\omega I_0(\nu_{\text{HI}}) \left( \frac{\nu}{\nu_{\text{HI}}} \right)^{-\alpha} e^{-\tau(\nu, \omega)}, \quad (\text{A2})$$

using the optical depth  $\tau(\nu, \omega)$  along a photon path  $s$  from the slab boundary to the point in the incident direction  $\omega$ :

$$\tau(\nu, \omega) = \sum_i \sigma_i(\nu) \int_{\omega} n_i ds, \quad (\text{A3})$$

where  $\sigma_i(\nu)$  and  $n_i$  are the photoionization cross section and the number density of the species  $i$  ( $= 1, 2, 3$  or HI, HeI, HeII, in the ascending order in its ionization energy), respectively. For simplicity, we approximate the cross sections by a single power-law:

$$\sigma_i(\nu) = \sigma_i(\nu_i) \left( \frac{\nu}{\nu_i} \right)^{-\eta_i} \Theta(\nu - \nu_i), \quad (\text{A4})$$

where  $\Theta(x)$  is the Heviside step function, and the amplitude  $\sigma_i(\nu_i)$ , the index  $\eta_i$ , and the ionization energy  $h\nu_i$  are taken from Osterbrock (1989) and listed in Table 6. Note that the following formalism can be readily extended and applied as long as cross sections are expressed as a superposition of power-laws.

Using the above expressions, the photoionization coefficients and heating rates for the species  $j$  are written as

$$\begin{aligned} \Gamma_j &= \int_{\nu_j}^{\infty} \frac{4\pi J(\nu)}{h\nu} \sigma_j(\nu) d\nu, \\ &= \frac{\sigma_j(\nu_j) I_0(\nu_j)}{h} \int d\omega \int_{\nu_j}^{\infty} \frac{d\nu}{\nu} \left( \frac{\nu}{\nu_j} \right)^{-\alpha-\eta_j} e^{-\tau(\nu, \omega)}, \end{aligned} \quad (\text{A5})$$

$$\begin{aligned}
\mathcal{H}_j &= \int_{\nu_j}^{\infty} \frac{4\pi J(\nu)}{h\nu} \sigma_j(\nu) (h\nu - h\nu_j) d\nu \\
&= h\nu_j \left[ \frac{\sigma_j(\nu_j) I_0(\nu_j)}{h} \int d\omega \int_{\nu_j}^{\infty} \frac{d\nu}{\nu_j} \left( \frac{\nu}{\nu_j} \right)^{-\alpha-\eta_j} e^{-\tau(\nu,\omega)} - \Gamma_j \right].
\end{aligned} \tag{A6}$$

Note that  $\mathcal{H}_j$  defined above is related to the heating rate per unit volume used in the main text (eq. [3]) by  $\mathcal{H} = \sum n_j \mathcal{H}_j$ . In general,  $\tau(\nu, \omega)$  is a complicated function of  $\nu$  as it is the sum of components with different spectral indices (eqs [A3],[A4]). However, the frequency integrations in equations (A5) and (A6) are separated into intervals as

$$\int_{\nu_j}^{\infty} d\nu \quad \longrightarrow \quad \sum_{i=j}^3 \int_{\nu_i}^{\nu_{i+1}} d\nu \quad \text{with } \nu_4 \equiv \infty, \tag{A7}$$

and it will not be a bad approximation to adopt for each interval

$$\tau(\nu, \omega) \simeq \tau(\nu_i, \omega) \left( \frac{\nu}{\nu_i} \right)^{-\eta_i^{\text{eff}}} \quad \text{at } \nu_i \leq \nu < \nu_{i+1}, \tag{A8}$$

where  $\tau(\nu_i, \omega)$  takes the sum over all species at  $\nu_i$  (eq.[A3]), while the effective index  $\eta_i^{\text{eff}}$  is set equal to the index  $\eta$  of the species which makes the dominant contribution to  $\tau(\nu_i, \omega)$ . Then the frequency integrations in equations (A5) and (A6) are performed analytically to give (see also Tajiri & Umemura 1998; Susa & Umemura 1999)

$$\begin{aligned}
\Gamma_j &= \frac{\sigma_j(\nu_j) I_0(\nu_j)}{h} \int d\omega \sum_{i=j}^3 \frac{1}{\eta_i^{\text{eff}}} \left\{ \frac{\gamma(\beta_{ji}, \tau(\nu_i, \omega))}{\tau^{\beta_{ji}}(\nu_i, \omega)} \left( \frac{\nu_i}{\nu_j} \right)^{-\beta_{ji} \eta_i^{\text{eff}}} \right. \\
&\quad \left. - \frac{\gamma(\beta_{ji}, \tilde{\tau}(\nu_{i+1}, \omega))}{\tilde{\tau}^{\beta_{ji}}(\nu_{i+1}, \omega)} \left( \frac{\nu_{i+1}}{\nu_j} \right)^{-\beta_{ji} \eta_i^{\text{eff}}} \right\},
\end{aligned} \tag{A9}$$

$$\begin{aligned}
\mathcal{H}_j &= h\nu_j \left[ \frac{\sigma_j(\nu_j) I_0(\nu_j)}{h} \int d\omega \sum_{i=j}^3 \frac{1}{\eta_i^{\text{eff}}} \left\{ \frac{\gamma(\beta'_{ji}, \tau(\nu_i, \omega))}{\tau^{\beta'_{ji}}(\nu_i, \omega)} \left( \frac{\nu_i}{\nu_j} \right)^{-\beta'_{ji} \eta_i^{\text{eff}}} \right. \right. \\
&\quad \left. \left. - \frac{\gamma(\beta'_{ji}, \tilde{\tau}(\nu_{i+1}, \omega))}{\tilde{\tau}^{\beta'_{ji}}(\nu_{i+1}, \omega)} \left( \frac{\nu_{i+1}}{\nu_j} \right)^{-\beta'_{ji} \eta_i^{\text{eff}}} \right\} - \Gamma_j \right],
\end{aligned} \tag{A10}$$

with

$$\beta_{ji} \equiv \frac{\alpha + \eta_j}{\eta_i^{\text{eff}}}, \quad \beta'_{ji} \equiv \frac{\alpha + \eta_j - 1}{\eta_i^{\text{eff}}}, \tag{A11}$$

where  $\tilde{\tau}(\nu_{i+1}, \omega)$  is an approximated optical depth computed by equation (A8) at its upper limit  $\nu_{i+1}$ , and  $\gamma(a, x)$  is the incomplete gamma function:

$$\gamma(a, x) \equiv \int_0^x e^{-t} t^{a-1} dt, \quad a > 0. \tag{A12}$$

In most astrophysically interesting cases,  $\beta > 0$  and  $\beta' > 0$  are both satisfied.

For a sufficiently long slab in a plane parallel symmetry with an arbitrary density profile, the optical depth given in equation (A3) varies with a direction cosine  $\mu = \cos \theta$  ( $\theta = 0$  if perpendicular to the plane) as

$$\begin{aligned}
\tau(\nu, \omega(\nu)) &= \frac{1}{\mu} \sum_i \sigma_i(\nu) N_i, \\
&= \frac{1}{\mu} \tau_{\perp}(\nu)
\end{aligned} \tag{A13}$$

where  $N_i = \int_{\theta=0} n_i ds$  is the column density perpendicular to the plane. Substituting equation (A13) into equations (A2), (A9), (A10), and taking  $\int d\omega \rightarrow 2\pi \int_0^1 d\mu$ , we obtain the following analytical formulae for the photons propagating from *one of the boundaries*:

$$J(\nu) = \frac{1}{2} I_0(\nu_{\text{HI}}) \left( \frac{\nu}{\nu_{\text{HI}}} \right)^{-\alpha} \left[ e^{-\tau_{\perp}(\nu)} - \tau_{\perp}(\nu) E_1(\tau_{\perp}(\nu)) \right], \quad (\text{A14})$$

$$\Gamma_j = \frac{2\pi\sigma_j(\nu_j)I_0(\nu_j)}{h} \sum_{i=j}^3 \frac{1}{\eta_i^{\text{eff}}} \left\{ f(\beta_{ji}, \tau_{\perp}(\nu_i)) \left( \frac{\nu_i}{\nu_j} \right)^{-\beta_{ji}\eta_i^{\text{eff}}} - f(\beta_{ji}, \tilde{\tau}_{\perp}(\nu_{i+1})) \left( \frac{\nu_{i+1}}{\nu_j} \right)^{-\beta_{ji}\eta_i^{\text{eff}}} \right\}, \quad (\text{A15})$$

$$\mathcal{H}_j = h\nu_j \left[ \frac{2\pi\sigma_j(\nu_j)I_0(\nu_j)}{h} \sum_{i=j}^3 \frac{1}{\eta_i^{\text{eff}}} \left\{ f(\beta'_{ji}, \tau_{\perp}(\nu_i)) \left( \frac{\nu_i}{\nu_j} \right)^{-\beta'_{ji}\eta_i^{\text{eff}}} - f(\beta'_{ji}, \tilde{\tau}_{\perp}(\nu_{i+1})) \left( \frac{\nu_{i+1}}{\nu_j} \right)^{-\beta'_{ji}\eta_i^{\text{eff}}} \right\} - \Gamma_j \right], \quad (\text{A16})$$

where  $\tilde{\tau}_{\perp}(\nu_{i+1}) = \tau_{\perp}(\nu_i)(\nu_{i+1}/\nu_i)^{-\eta_i^{\text{eff}}}$ , and a function  $f(a, x)$  is defined by

$$f(a, x) = \frac{1}{a+1} \left[ \frac{\gamma(a, x)}{x^a} + e^{-x} - xE_1(x) \right], \quad (\text{A17})$$

$$\rightarrow \begin{cases} \frac{1}{a} & (x \rightarrow 0), \\ \frac{1}{a+1} \frac{\Gamma(a)}{x^a} & (x \rightarrow \infty). \end{cases} \quad (\text{A18})$$

using the incomplete gamma function (eq. [A12]) and the exponential integral:

$$E_n(x) = x^{n-1} \int_x^{\infty} \frac{e^{-t}}{t^n} dt, \quad x > 0, \quad n = 0, 1, 2, \dots \quad (\text{A19})$$

The above results show that one can explicitly compute the photoionization coefficients and heating rates, once given the column densities perpendicular to the plane. In the optically thick limit  $\tau_{\perp} \rightarrow \infty$ , the photoionization coefficients and heating rates vary as  $\tau_{\perp}^{-\beta}$  (see also eqs [A24][A25] below).

## A.2. Simple example – pure hydrogen gas –

If the gas is dominated by a single species, say atomic hydrogen, the expressions derived above can be reduced to even simpler forms as presented below. Such formulae are also quite useful in making physical estimations in many astrophysical problems.

For the pure hydrogen gas, the effective indices  $\eta_i^{\text{eff}}$  can be all set equal to  $\eta_{\text{HI}}^{\text{eff}} = \eta_{\text{HI}}$ , and equations (A15) and (A16) reduce to

$$\Gamma_{\text{HI}} = \frac{2\pi\sigma_{\text{HI}}(\nu_{\text{HI}})I_0(\nu_{\text{HI}})}{h} \frac{f(\beta_{\text{HI}}, \tau_{\perp}(\nu_{\text{HI}}))}{\eta_{\text{HI}}}, \quad (\text{A20})$$

$$\mathcal{H}_{\text{HI}} = h\nu_{\text{HI}} \left[ \frac{2\pi\sigma_{\text{HI}}(\nu_{\text{HI}})I_0(\nu_{\text{HI}})}{h} \frac{f(\beta'_{\text{HI}}, \tau_{\perp}(\nu_{\text{HI}}))}{\eta_{\text{HI}}} - \Gamma_{\text{HI}} \right], \quad (\text{A21})$$

with  $\eta_{\text{HI}} = 3$ ,  $\beta_{\text{HI}} = (\alpha + 3)/3$ , and  $\beta'_{\text{HI}} = (\alpha + 2)/3$ . Given a specific value of  $\alpha$ , these expressions are computed using equation (A18) in the optically thin and thick limits as



1. optically thin limit:  $\tau_{\perp}(\nu_{\text{HI}}) \rightarrow 0$

$$\Gamma_{\text{HI}} = \begin{cases} 1.49 \times 10^{-12} I_{21} & \text{s}^{-1} & (\alpha = 1), \\ 7.47 \times 10^{-13} I_{21} & \text{s}^{-1} & (\alpha = 5), \end{cases} \quad (\text{A22})$$

$$\mathcal{H}_{\text{HI}} = \begin{cases} 1.08 \times 10^{-23} I_{21} & \text{erg s}^{-1} & (\alpha = 1), \\ 2.33 \times 10^{-24} I_{21} & \text{erg s}^{-1} & (\alpha = 5), \end{cases} \quad (\text{A23})$$

2. optically thick limit:  $\tau_{\perp}(\nu_{\text{HI}}) \rightarrow \infty$

$$\Gamma_{\text{HI}} = \begin{cases} 7.62 \times 10^{-13} I_{21} \tau_{\perp}^{-4/3}(\nu_{\text{HI}}) & \text{s}^{-1} & (\alpha = 1), \\ 8.18 \times 10^{-13} I_{21} \tau_{\perp}^{-8/3}(\nu_{\text{HI}}) & \text{s}^{-1} & (\alpha = 5), \end{cases} \quad (\text{A24})$$

$$\mathcal{H}_{\text{HI}} = \begin{cases} 2.17 \times 10^{-23} I_{21} \tau_{\perp}^{-1}(\nu_{\text{HI}}) & \text{erg s}^{-1} & (\alpha = 1), \\ 1.55 \times 10^{-23} I_{21} \tau_{\perp}^{-7/3}(\nu_{\text{HI}}) & \text{erg s}^{-1} & (\alpha = 5), \end{cases} \quad (\text{A25})$$

where  $I_{21} = I_0(\nu_{\text{HI}})/(10^{-21} \text{erg s}^{-1} \text{cm}^{-2} \text{str}^{-1} \text{Hz}^{-1})$ . Note that equations (A20)– (A25) take account of the photons propagating from only *one of the boundaries*. In particular, the expressions in the optically thin limit (eqs [A22] [A23]) should be multiplied by 2 to incorporate the photons coming from all directions.

From the above results, one can readily estimate the ionizing structure of a medium exposed to the external photoionizing flux. We restrict our attention to the gas of temperature  $T \sim 10^4 \text{K}$  and ignore the collisional ionization. Then the ionization balance is expressed as

$$\Gamma_{\text{HI}} X_{\text{HI}} \sim \alpha_{\text{H}} n_{\text{H}} (1 - X_{\text{HI}})^2, \quad (\text{A26})$$

where

$$\alpha_{\text{H}} \simeq 3.96 \times 10^{-13} T_4^{-0.7} \text{cm}^3 \text{s}^{-1}, \quad (\text{A27})$$

is the hydrogen recombination rate to the ground level (Spitzer 1978; Fukugita & Kawasaki 1994), and  $T_4 \equiv T/10^4 \text{K}$ . Inserting equations (A22) and (A24) into (A26), we obtain

1. optically thin limit:  $\tau_{\perp}(\nu_{\text{HI}}) \rightarrow 0$

$$\frac{X_{\text{HI}}}{(1 - X_{\text{HI}})^2} \sim \begin{cases} 0.133 I_{21}^{-1} n_1 T_4^{-0.7} & (\alpha = 1), \\ 0.265 I_{21}^{-1} n_1 T_4^{-0.7} & (\alpha = 5), \end{cases} \quad (\text{A28})$$

2. optically thick limit:  $\tau_{\perp}(\nu_{\text{HI}}) \rightarrow \infty$

$$\frac{X_{\text{HI}}}{(1 - X_{\text{HI}})^2} \sim \begin{cases} 0.520 I_{21}^{-1} n_1 T_4^{-0.7} \tau_{\perp}^{4/3}(\nu_{\text{HI}}) & (\alpha = 1), \\ 0.484 I_{21}^{-1} n_1 T_4^{-0.7} \tau_{\perp}^{8/3}(\nu_{\text{HI}}) & (\alpha = 5), \end{cases} \quad (\text{A29})$$

where  $n_1 \equiv n_{\text{H}}/\text{cm}^{-3}$ , and we have multiplied equation (A22) by a factor 2 to incorporate the photons coming from all directions.

### References

- Anderson, S. F., Hogan, C. J., Williams, B. F., & Carswell, R. F. 1999, *AJ*, 117, 56
- Anninos, W. Y., & Norman, M. L. 1994, *ApJ*, 429, 434
- Babul, A., & Rees, M. J. 1992, *MNRAS*, 255, 346
- Babul, A., & Ferguson, H. C. 1996, *ApJ*, 458, 100
- Baljtlik, S., Duncan, R. C., & Ostriker, J. P. 1988, *ApJ*, 327, 570
- Barkana, R., & Loeb, A. 1999, *ApJ* in press.
- Barns J., & Efstathiou, G. 1987, *ApJ*, 319, 575
- Bechtold, J. 1994, *ApJS*, 91, 1
- Berger, A. J., et al. 1998, *Nature*, 394, 248
- Bertschinger, E. 1985, *ApJS*, 58, 39
- Bond, J. R., Szalay, A. S., & Silk, J. 1988, *ApJ*, 324, 627
- Bond, J. R., Cole, S., Efstathiou, G., & Kaiser, N. 1991, *ApJ*, 379, 440
- Bowers, R. L., & Wilson, J. R. 1991, *Numerical Modeling in Applied Physics and Astrophysics* (Boston: Jones & Bartlett)
- Cen, R. 1992, *ApJS*, 78, 341
- Cen, R., & Ostriker, J. P. 1992, *ApJ*, 393, 22
- Cen, R., & Ostriker, J. P. 1999, *ApJ*, 514, 1
- Chengalur, J. N., & Kanekar, N. 1999, *MNRAS*, 302, L29
- Chiba, M., & Nath B. B. 1994, *ApJ*, 436, 618
- Chieze, J.-P., Teyssier, R., & Alimi, J.-M. 1997, *ApJ*, 484, 40
- Cole, S., Aragon-Salamanca, A., Frenk, C. S., Navarro, J. F., & Zepf, S. E. 1994, *MNRAS*, 271, 744
- Connolly, A. J., Szalay, A. S., Dickinson, M., Subbarao, M. U., & Brunner, R. J. 1997, *ApJ*, 486, L11
- Cooke, A. J., Espey, B., & Carswell, R. F. 1997, *MNRAS*, 284, 552
- Couchman, H. M. P. 1985, *MNRAS*, 214, 137
- Couchman, H. M. P., & Rees, M. J. 1986, *MNRAS*, 221, 53
- Efstathiou, G. 1992, *MNRAS*, 256, 43
- Efstathiou, G. & Jones, B. J. T. 1979, *MNRAS*, 186, 133
- Eke, V. R., Cole, S., & Frenk, C. S. 1996, *MNRAS*, 282, 263
- Fukugita, M., & Kawasaki, M. 1994, *MNRAS*, 269, 563
- Giallongo, E., Cristiani, S., D’Odorico, S., Fontana, A., & Savaglio, S. 1996, *ApJ*, 466, 46

- Gnedin, N. Y., Ostriker, J. P. 1997, ApJ, 486, 581
- Gott, J. R. III 1975, ApJ, 201, 296
- Gunn, J. E., & Peterson, B. A. 1965, ApJ, 142, 1633
- Haiman, Z., & Loeb, A. 1998, ApJ, 503, 505
- Haiman, Z., Thoul, A. A., & Loeb, A. 1996, ApJ, 464, 523
- Haiman, Z., Rees, M. J., & Loeb, A. 1996, ApJ, 467, 522
- Haiman, Z., Rees, M. J., & Loeb, A. 1997, ApJ, 476, 458
- Hogan, C. J., Anderson, S. F. & Rugers, M. H. 1997, AJ, 113, 1495
- Hughes, D., et al. 1998, Nature, 398, 241
- Ikeuchi, S. 1986, Ap&SS, 118, 509
- Ikeuchi, S., Murakami, I., & Rees, M. J. 1988, MNRAS, 236, 21P
- Ikeuchi, S., Murakami, I., & Rees, M. J. 1989, PASJ, 41, 1095
- Kauffmann, G., White, S. D. M., & Guiderdoni, B. 1993, MNRAS, 264, 201
- Kepner, J., Babul, A., & Spergel, N. 1997, ApJ, 487, 61
- Kitayama, T., & Suto, Y. 1996a, MNRAS, 280, 638
- Kitayama, T., & Suto, Y. 1996b, ApJ, 469, 480
- Kitayama, T., & Suto, Y. 1997, ApJ, 490, 557
- Lacey, C. G., & Cole, S. 1993, MNRAS, 262, 627
- Lilly, S. J., Le Fèvre, O., Hammer, F., Crampton, D. 1996, ApJ, 460, L1
- Lane, W., Smette, A., Briggs, F., Rao, S., Turnshek, D., & Meylan, G. 1998, ApJ, 116, 26
- Madau, P., Ferguson, H. C., Dickinson, M. E., Giavalisco M., Steidel, C. C., & Fruchter, A. 1996, MNRAS, 283, 1388
- Madau, P., Haardt, F., & Rees, M. J. 1999, ApJ, 514, 648
- Madau, P., Pozzetti, L., & Dickinson, M. 1998, ApJ, 498, 106
- Manrique, A., & Salvador-Sole, E. 1996, ApJ, 467, 504
- Miralda-Escudé J., & Ostriker, J. P. 1990, ApJ, 350, 1
- Murakami, I., & Ikeuchi, S. 1990, PASJ, 42, L11
- Murakami, I., & Ikeuchi, S. 1993, ApJ, 409, 42
- Navarro, J. F., & Steinmetz, M. 1997, ApJ, 478, 13
- Okoshi, K. & Ikeuchi, S. 1996, PASJ, 48, 441
- Osterbrock, D. E. 1989, Astrophysics of Gaseous Nebulae and Active Galactic Nuclei (Mill Valley: University Science Books)

- Padmanabham, T. 1993, *Structure Formation in the Universe* (Cambridge: Cambridge Univ. Press)
- Pettini, M., Kellog, M., Steidel, C. C., Dickinsonl, M., Adelberger, K. L., & Giavalisco, M. 1998, *ApJ*, 508, 539
- Press, W. H., & Schechter, P. 1974, *ApJ*, 187, 425
- Quinn, T., Katz, N., & Efstathiou, G. 1996, *MNRAS*, 278, L49
- Rauch, M. 1998, *ARA&A*, 36, 267
- Rees, M. J. 1986, *MNRAS*, 218, 25P
- Reimers, D., Köhler, S., Wisotzki, L., Groote, D., Rodriguez-Pascual, P., & Wamsteker, W. 1997, *A&A*, 327, 890
- Richtmyer, R., & Morton, K. W. 1967, *Difference Methods for Initial-Value Problems* (New York: Interscience)
- Sargent, W. L. W., Young, P. J., Boksenberg, A. & Tytler, D. 1980, *ApJS*, 42, 41
- Sasaki, S. 1994, *PASJ*, 46, 427
- Savaglio, S., Cristiani, S., D’Odorico, S., Fontana, A., Giallongo, E., & Molaro, P. 1997, *A&A*, 318;347
- Smail, I., Ivison, R. J., & Blain, A. W. 1997, *ApJ*, 490, L5
- Spitzer, L. Jr. 1978, *Physical Processes in the Intergalactic Medium* (Wiley: New York)
- Spitzer, L. Jr., & Hart, M. H. 1971, *ApJ*, 166, 483
- Susa, H., & Umemura, M. 1999, *ApJ* submitted.
- Tajiri, Y., & Umemura, M. 1998, *ApJ*, 502, 59
- Thoul, A. A., & Weinberg, D. H. 1995, *ApJ*, 442, 480
- Thoul, A. A., & Weinberg, D. H. 1996, *ApJ*, 465, 608
- Totani, T., Yoshii, Y., & Sato, K. 1997, *ApJ*, 483, L75
- Umemura, M. 1993, *ApJ*, 406, 361
- Umemura, M., & Ikeuchi, S. 1984, *Prog. Theor. Phys.*, 72, 47
- Umemura, M., & Ikeuchi, S. 1985, *ApJ*, 299, 583
- Vedel, H., Hellsten U., & Sommer-Larsen J. 1994, *MNRAS*, 1994, 271
- Viana, P. T. P., & Liddle, A. R. 1996, *MNRAS*, 281, 323
- Warren, M. S., Quinn, P. J., Salmon, J. K., & Zurek, W. H. 1992, *ApJ*, 399, 405
- Weinberg, D., Hernquist, L., & Katz, N. 1997, *ApJ*, 477, 8
- White, S. D. M., & Frenk, C. S. 1991, *ApJ*, 379, 52
- Zhang, Y., Anninos, P., & Norman, M. L. 1995, *ApJ*, 453, L57

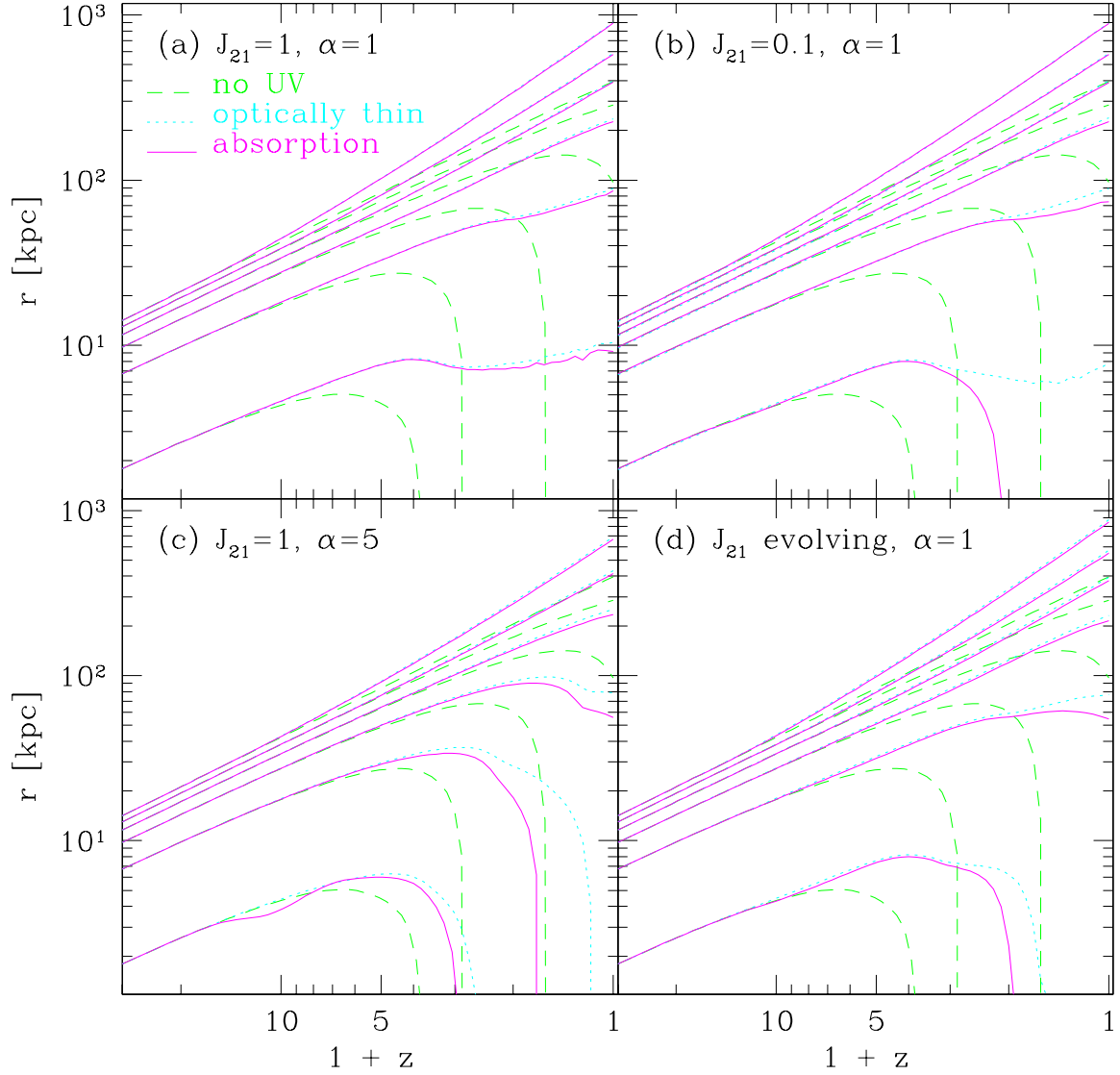


Fig. 1.— Trajectories of radii of gas shells enclosing 0.2 (inner-most shell), 10, 30, 50, 70, 90 % of  $M_{\text{bound}}$  in the low-redshift collapse ( $z_c = 0.5$ ) for a cloud with  $V_c = 32 \text{ km s}^{-1}$  ( $M_{\text{cloud}} \simeq 9 \times 10^8 M_{\odot}$ ) and different parameters of the UV background; (a)  $J_{21} = 1, \alpha = 1$ , (b)  $J_{21} = 0.1, \alpha = 1$ , (c)  $J_{21} = 1, \alpha = 5$ , and (d) evolving  $J_{21}, \alpha = 1$ . Different lines indicate the no UV case (dashed), the optically thin case (dotted), and the case with absorption (solid).

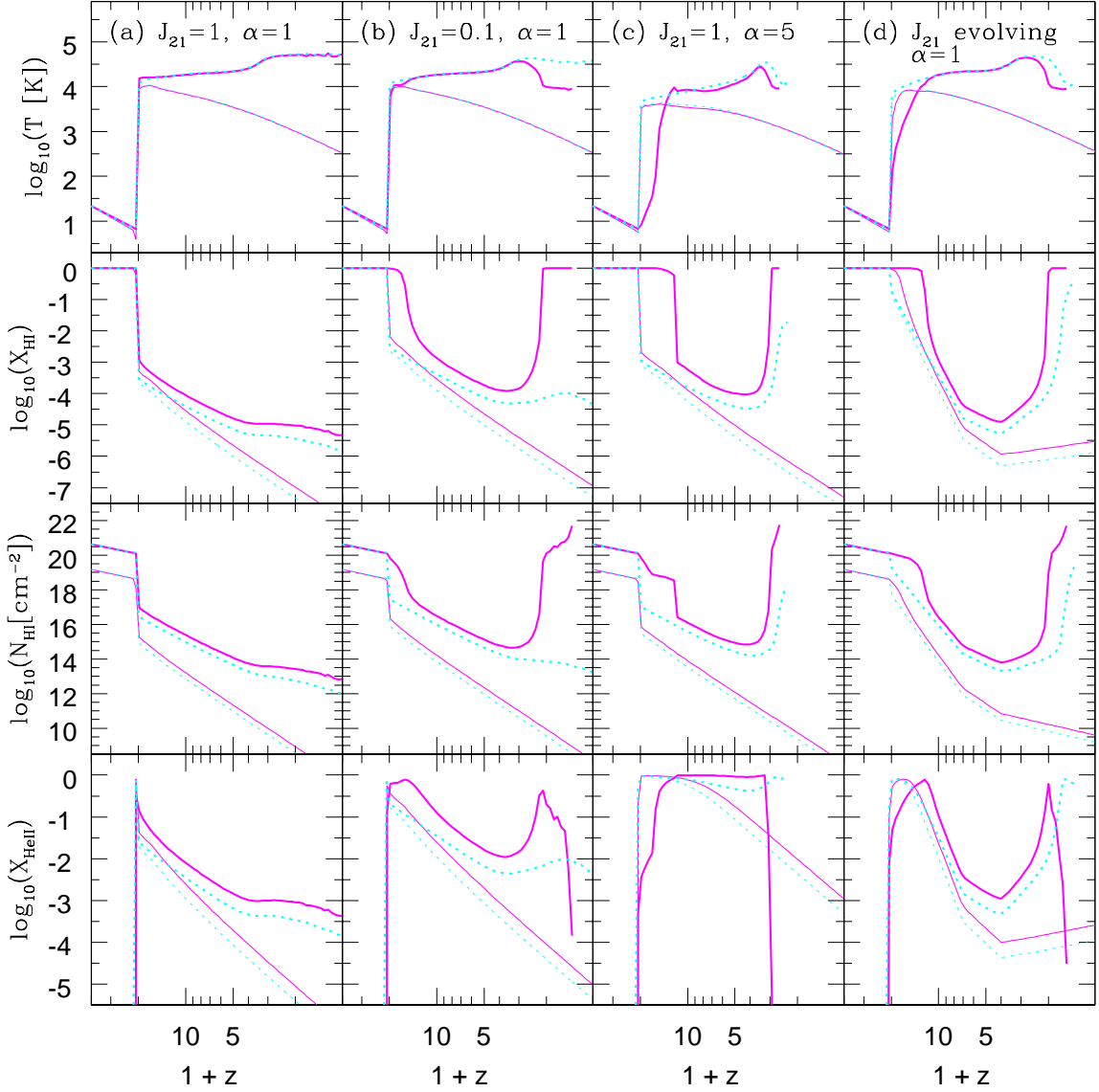


Fig. 2.— Evolution of temperature (highest panels),  $X_{\text{HI}}$  (second highest),  $N_{\text{HI}}$  (second lowest), and  $X_{\text{HeII}}$  (lowest) of gas shells enclosing 0.2% (thick lines) and 90% (thin lines) of  $M_{\text{bound}}$  in the low-redshift collapse ( $z_c = 0.5$ ) for a cloud with  $V_c = 32 \text{ km s}^{-1}$ . (a)  $J_{21} = 1$ ,  $\alpha = 1$ , (b)  $J_{21} = 0.1$ ,  $\alpha = 1$ , (c)  $J_{21} = 1$ ,  $\alpha = 5$ , and (d) evolving  $J_{21}$ ,  $\alpha = 1$ . Different lines indicate the optically thin case (dotted lines) and the case with absorption (solid lines).

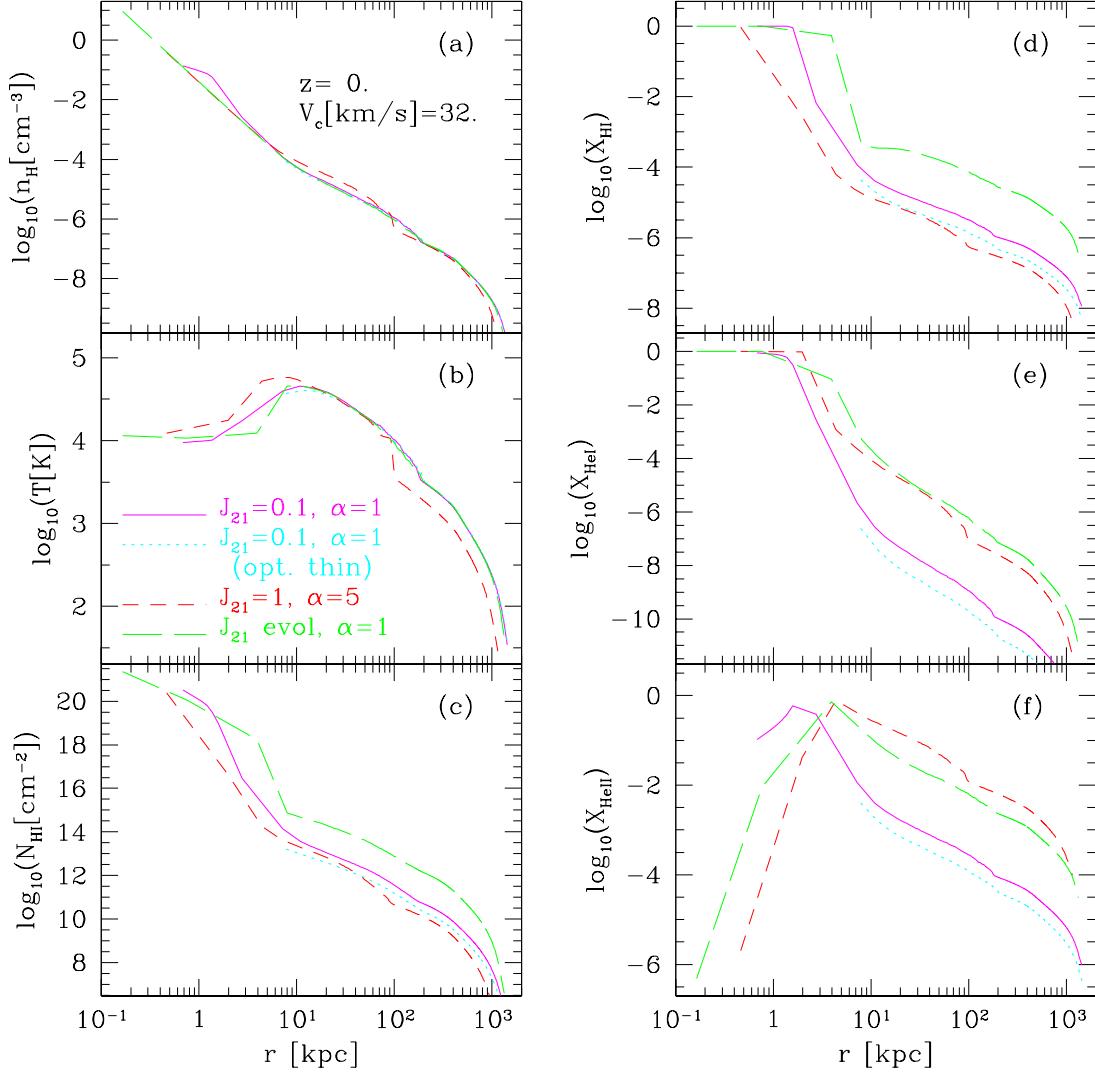


Fig. 3.— Radial profiles at  $z = 0$  of (a) hydrogen density, (b) temperature, (c) HI column density from the boundary, (d)  $X_{\text{HI}}$ , (e)  $X_{\text{HeI}}$ , and (f)  $X_{\text{HeII}}$  in the low-redshift collapse ( $z_c = 0.5$ ) for a cloud with  $V_c = 32 \text{ km s}^{-1}$ . Lines correspond to different parameters of the UV background as shown in the figure (unless indicated explicitly, absorption is taken into account).

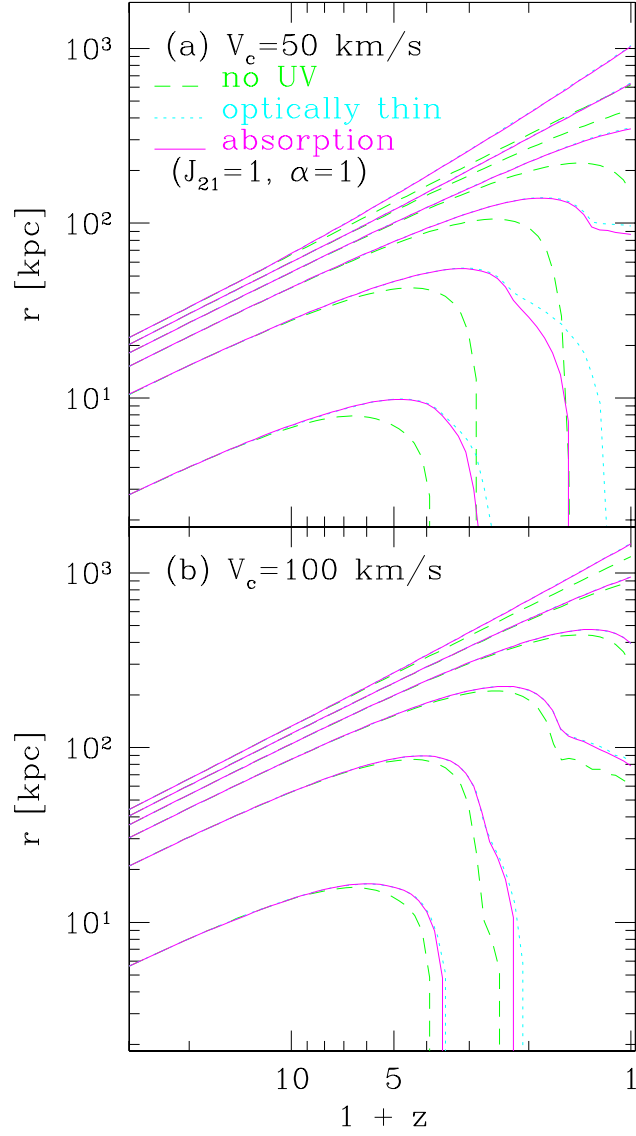


Fig. 4.— Same as Fig. 1, except for a cloud with (a)  $V_c = 50$  km s $^{-1}$  ( $M_{\text{cloud}} \simeq 3 \times 10^9 M_\odot$ ), and (b)  $V_c = 100$  km s $^{-1}$  ( $M_{\text{cloud}} \simeq 3 \times 10^{10} M_\odot$ ), in the case of  $J_{21} = 1$  and  $\alpha = 1$ .



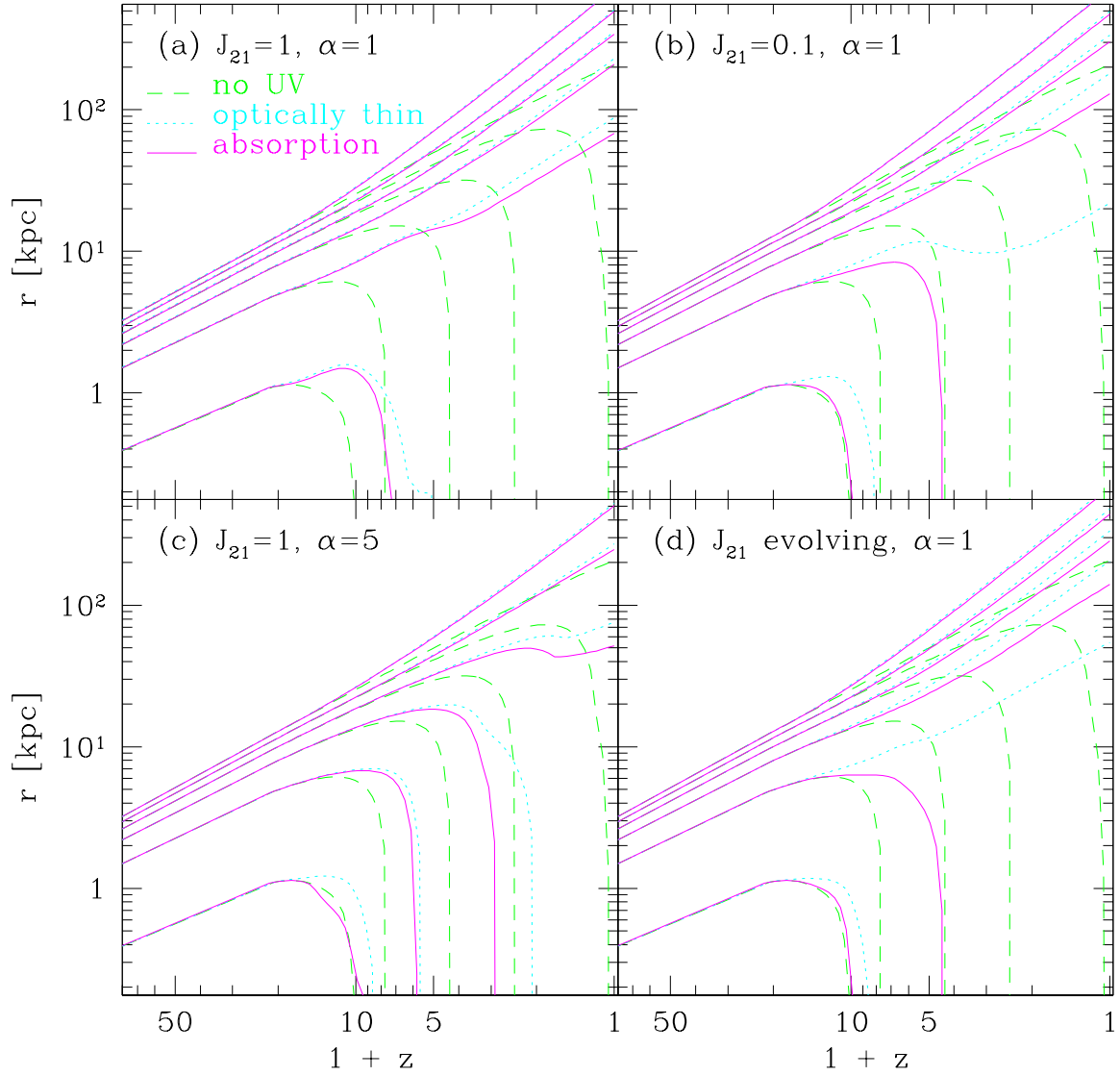


Fig. 5.— Same as Fig. 1, except for the middle-redshift collapse ( $z_c = 3$ ) with  $V_c = 32 \text{ km s}^{-1}$  ( $M_{\text{cloud}} \simeq 2 \times 10^8 M_\odot$ ).

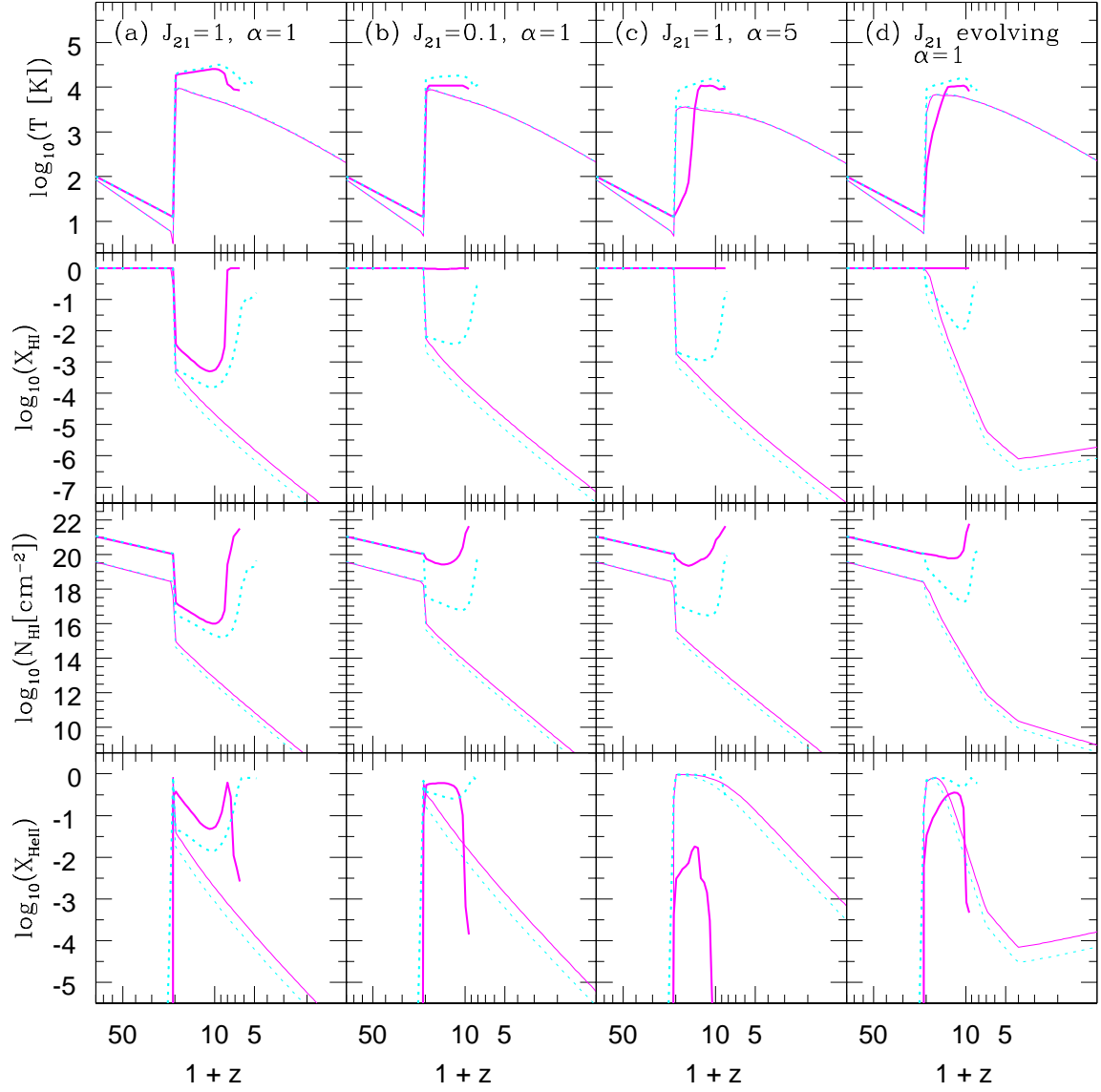


Fig. 6.— Same as Fig. 2, except for the middle-redshift collapse ( $z_c = 3$ ) with  $V_c = 32 \text{ km s}^{-1}$  ( $M_{\text{cloud}} \simeq 2 \times 10^8 M_{\odot}$ ).

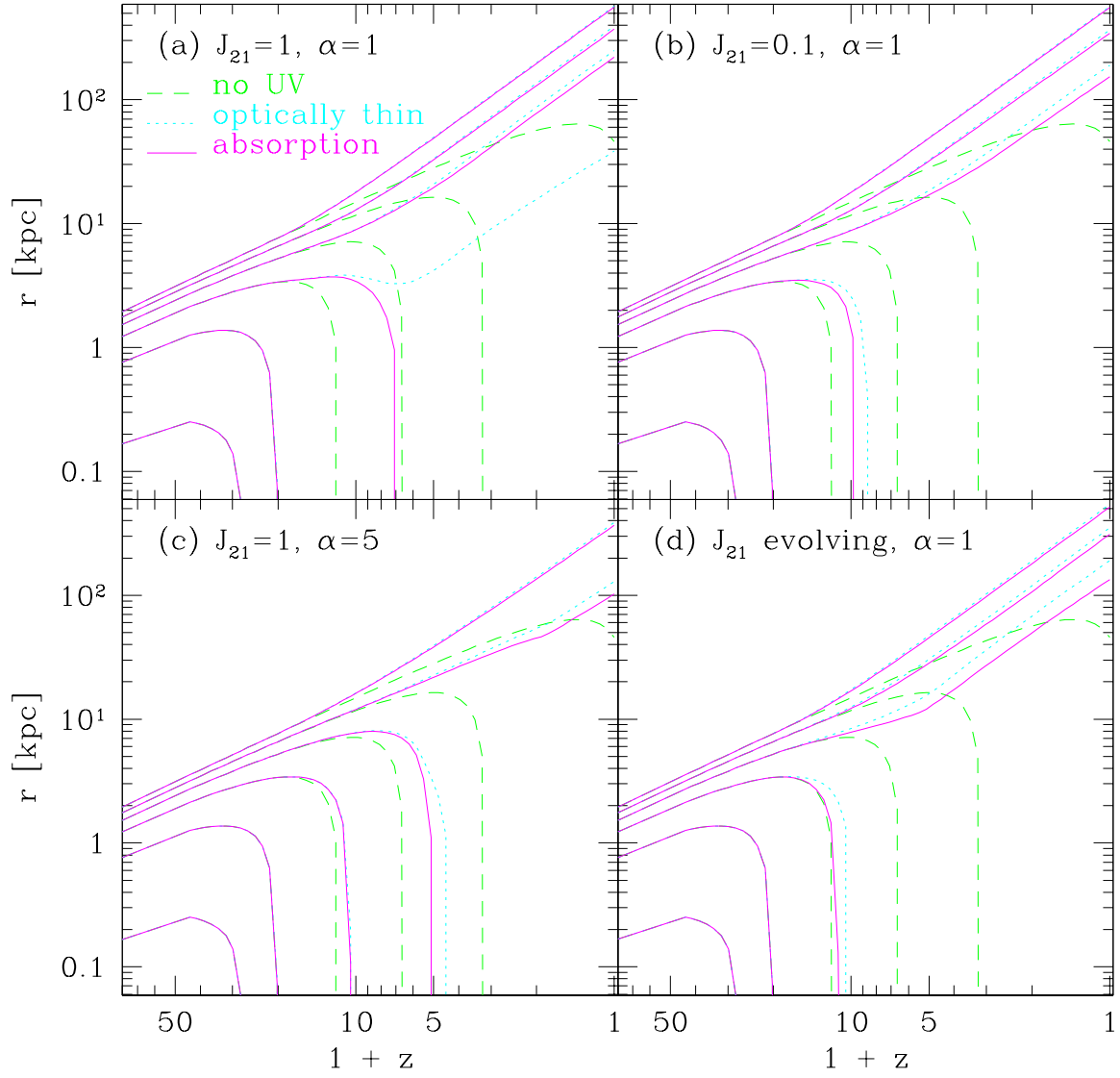


Fig. 7.— Same as Fig. 1, except for the high-redshift collapse ( $z_c = 10$ ) with  $V_c = 32 \text{ km s}^{-1}$  ( $M_{\text{cloud}} \simeq 5 \times 10^7 M_{\odot}$ ).

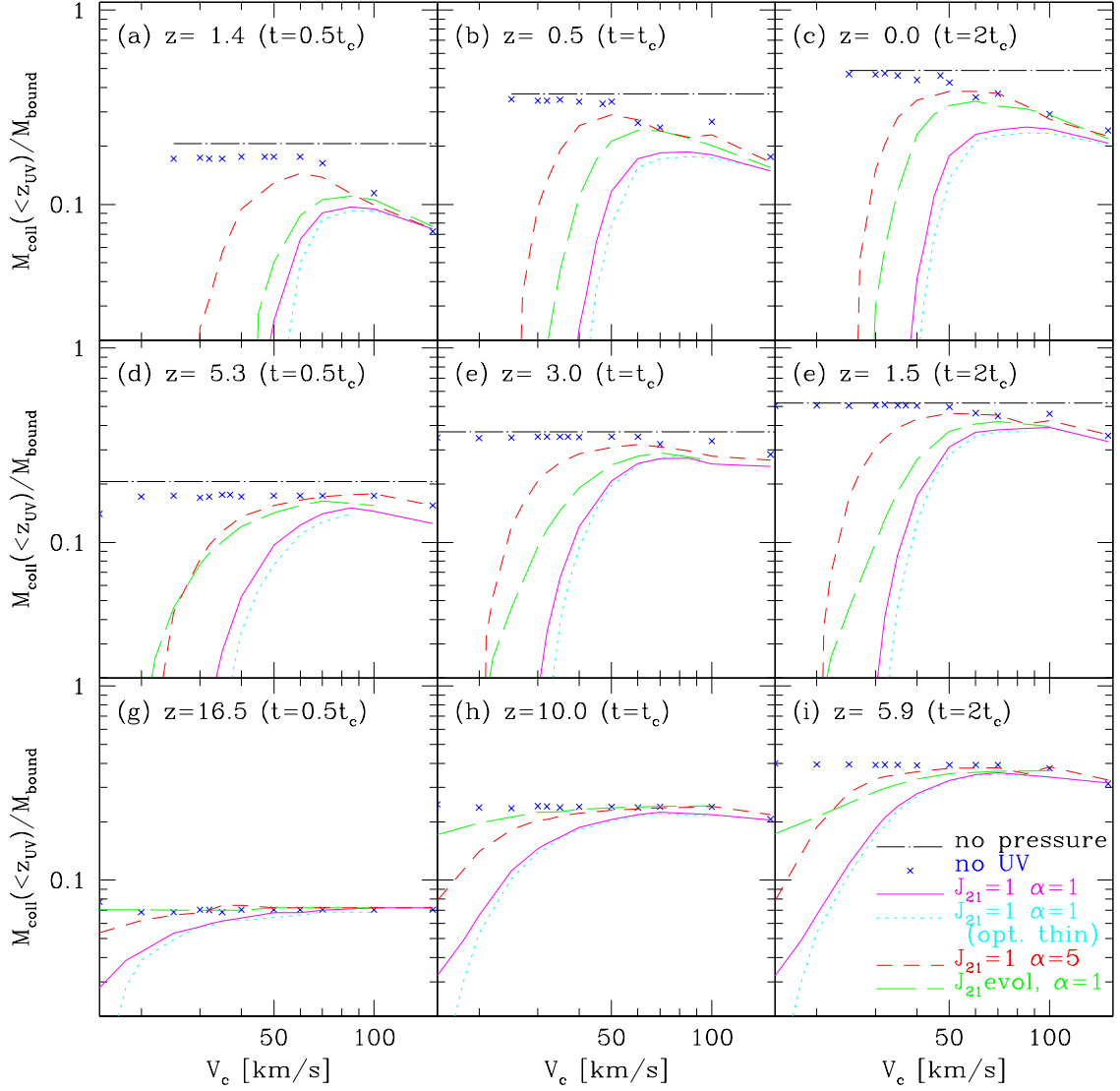


Fig. 8.— The fraction of gas mass collapsed after the onset of the UV background  $z_{\text{UV}} = 20$  as a function of circular velocity. Each horizontal row traces the time evolution at  $t = 0.5t_c$ ,  $t_c$ ,  $2t_c$  of runs with  $z_c = 0.5$  (top panels), 3 (middle), and 10 (bottom). Lines and symbols correspond to different parameters of the UV background as shown in the figure (unless indicated, absorption is considered).

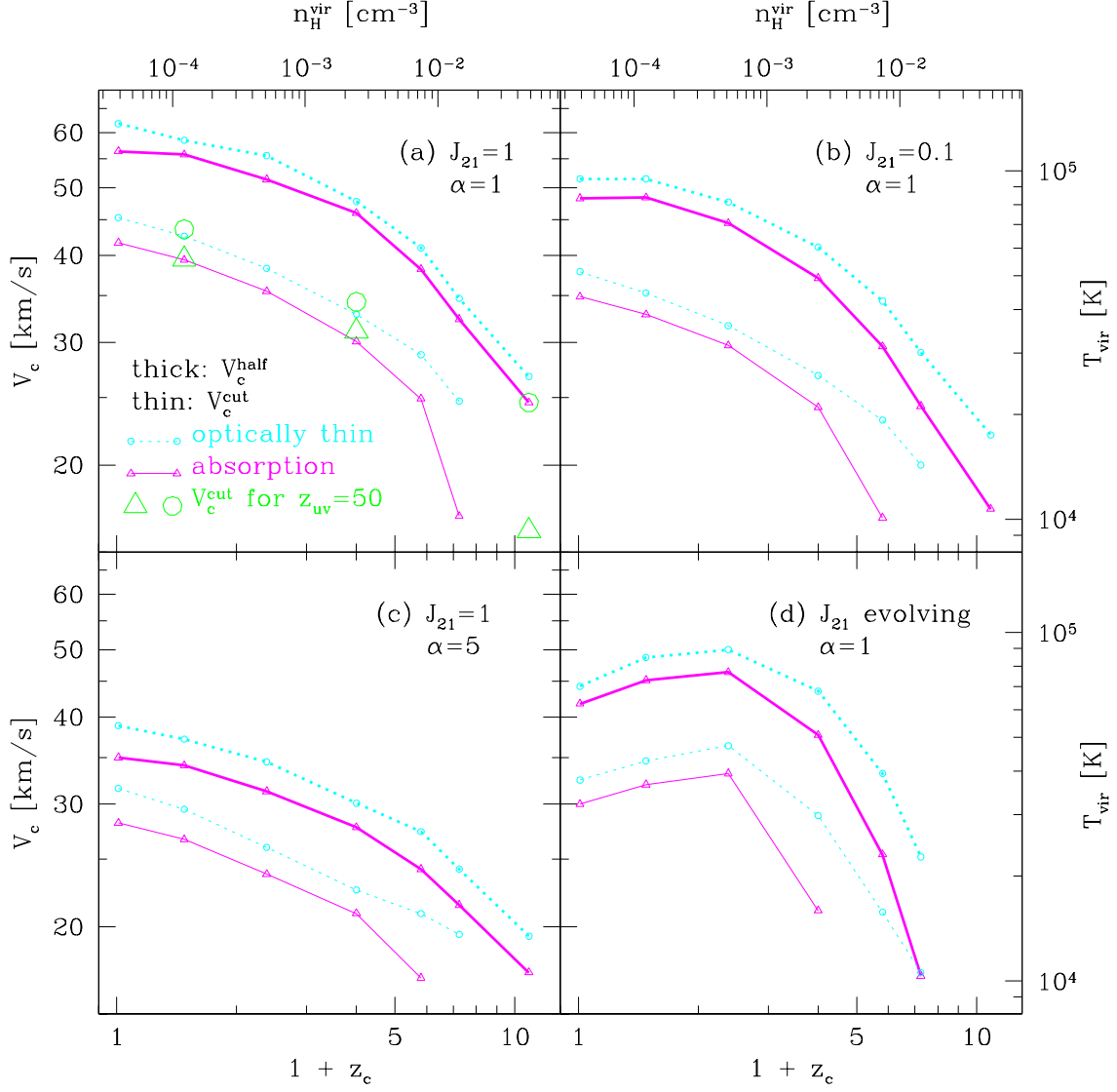


Fig. 9.— The critical circular velocity  $V_c^{\text{cut}}$  (thin lines) and  $V_c^{\text{half}}$  (thick lines) of the collapse (see text for definitions) with absorption (triangles, solid lines) and in the optically thin case (circles, dotted lines). (a)  $J_{21} = 1$ ,  $\alpha = 1$ , (b)  $J_{21} = 0.1$ ,  $\alpha = 1$ , (c)  $J_{21} = 1$ ,  $\alpha = 5$ , and (d) evolving  $J_{21}$ ,  $\alpha = 1$ . Larger symbols in panel (a) indicate  $V_c^{\text{cut}}$  in the case of  $z_{\text{UV}} = 50$ .

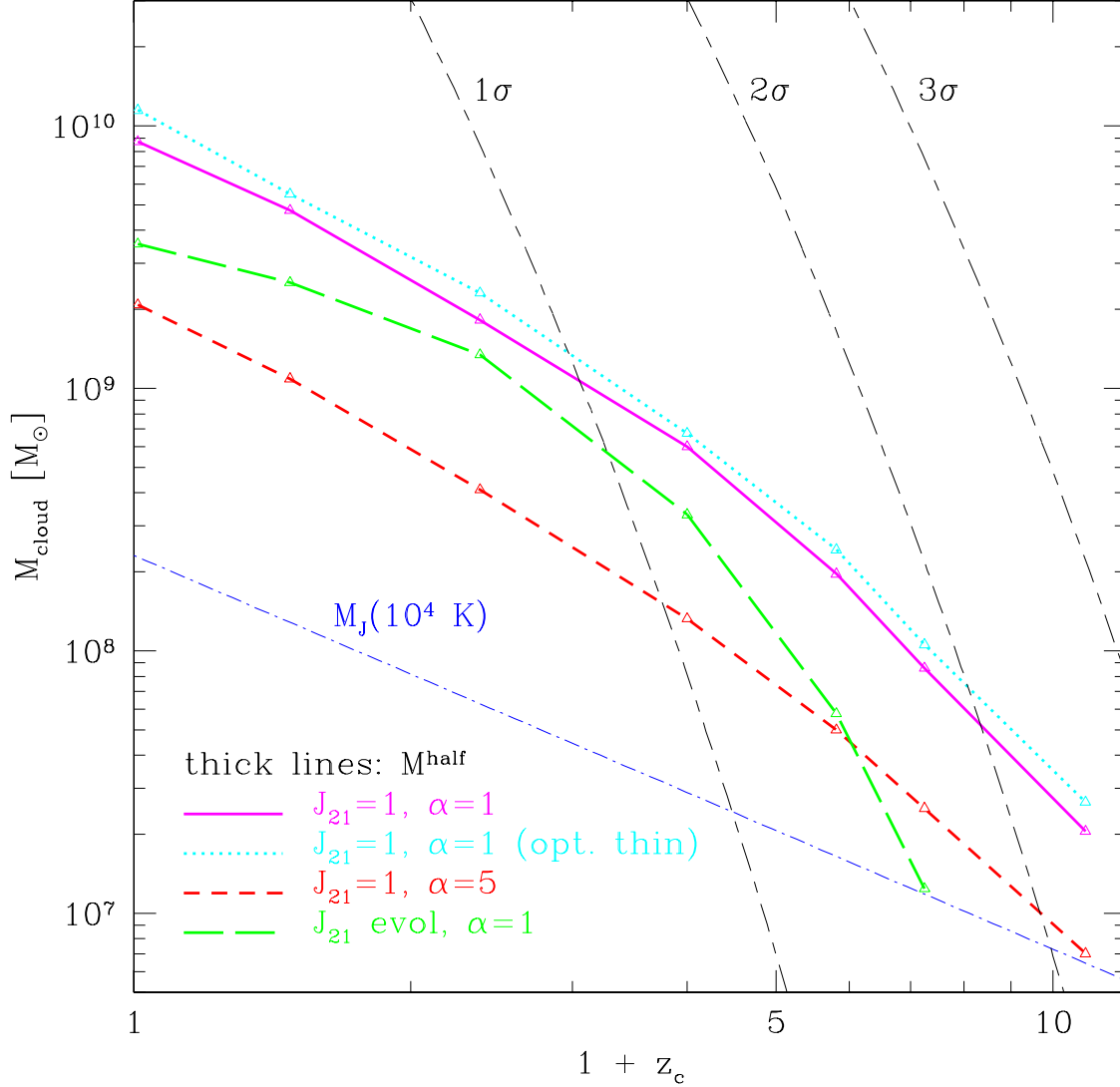


Fig. 10.— The baryon mass corresponding to  $V_c^{\text{half}}$  as a function of collapse epoch  $z_c$  (thick lines). Different parameters of the UV background are assumed as shown in the figure (unless indicated, absorption is considered). Also plotted are the Jeans mass with  $T = 10^4 \text{ K}$  (thin dot-short-dashed lines) and the masses corresponding to 1,2,3 $\sigma$  density perturbations (thin dot-long-dashed lines) in the standard CDM universe with  $\Omega_0 = 1$ ,  $h = 0.5$ ,  $\Omega_b = 0.1$ , and  $\sigma_8 = 0.6$ .

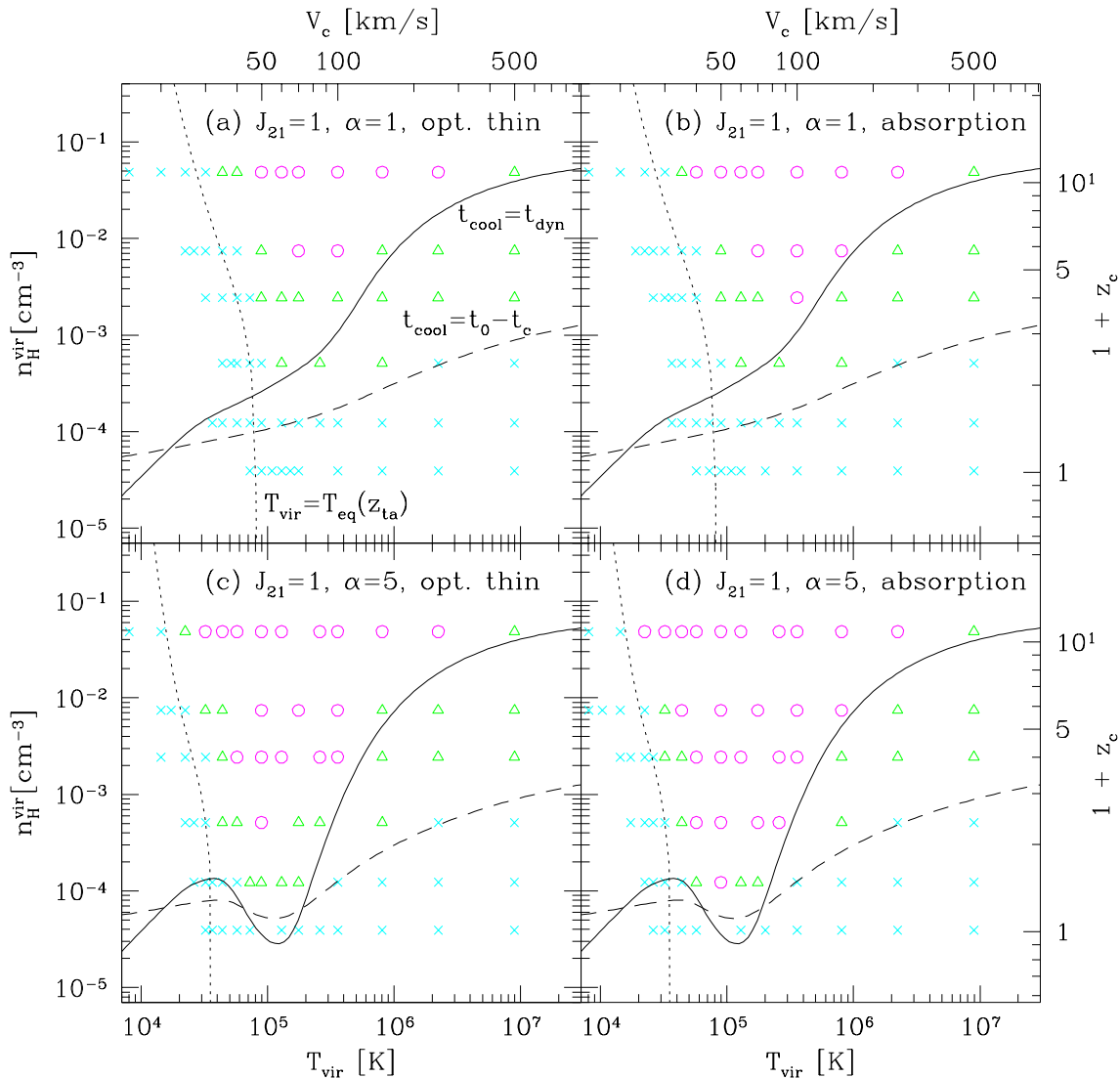


Fig. 11.— Density–temperature diagrams from our simulations and analytical estimates. Symbols indicate the virial density and temperature of simulated clouds in which the cooled gas mass reaches  $M_{\text{cloud}}$  before  $t_c + t_{\text{dyn}}$  (circles), before the present age of the universe  $t_0$  (triangles), and otherwise (crosses); (a)  $J_{21} = 1$ ,  $\alpha = 1$ , optically thin case, (b)  $J_{21} = 1$ ,  $\alpha = 1$ , with absorption, (c)  $J_{21} = 1$ ,  $\alpha = 5$ , optically thin case, and (d)  $J_{21} = 1$ ,  $\alpha = 5$ , with absorption. Lines show the analytic relations  $t_{\text{cool}} = t_{\text{dyn}}$  evaluated at  $z_c$  (solid),  $t_{\text{cool}} = t_0 - t_c$  at  $z_c$  (dashed), and  $T_{\text{vir}} = T_{\text{eq}}$  at  $z_{\text{ta}}$ , with the same UV parameters as the simulations except for assuming that the medium is optically thin in all cases.

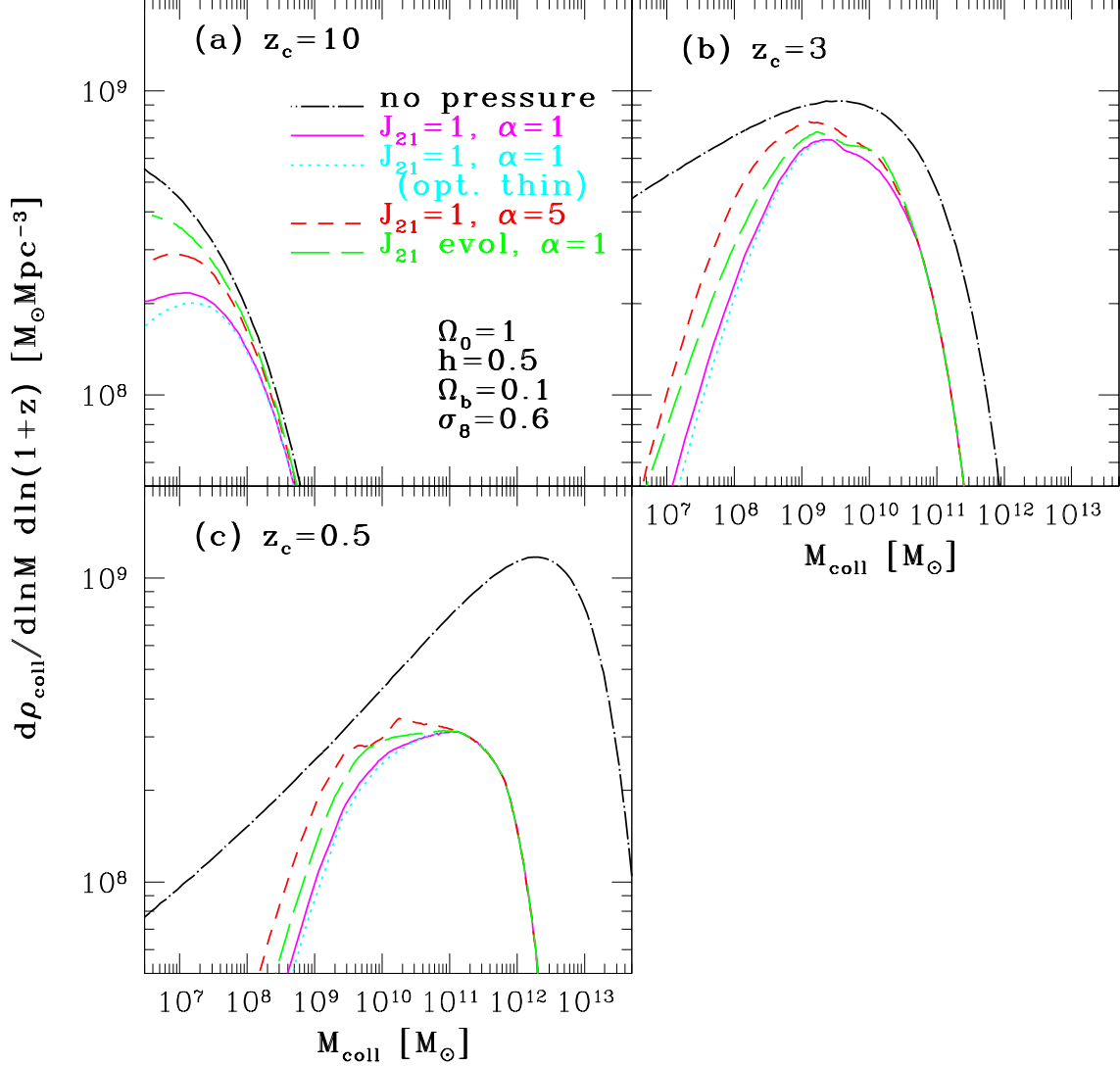


Fig. 12.— Mass distribution of the baryon density that collapses per Hubble time at (a)  $z_c = 10$ , (b)  $z_c = 3$ , and (c)  $z_c = 0.5$  in the standard CDM model with  $\Omega_0 = 1$ ,  $h = 0.5$ ,  $\Omega_b = 0.1$ , and  $\sigma_8 = 0.6$ . Lines indicate the cases of different UV parameters or of no pressure as shown in the figure (unless indicated, absorption is taken into account).



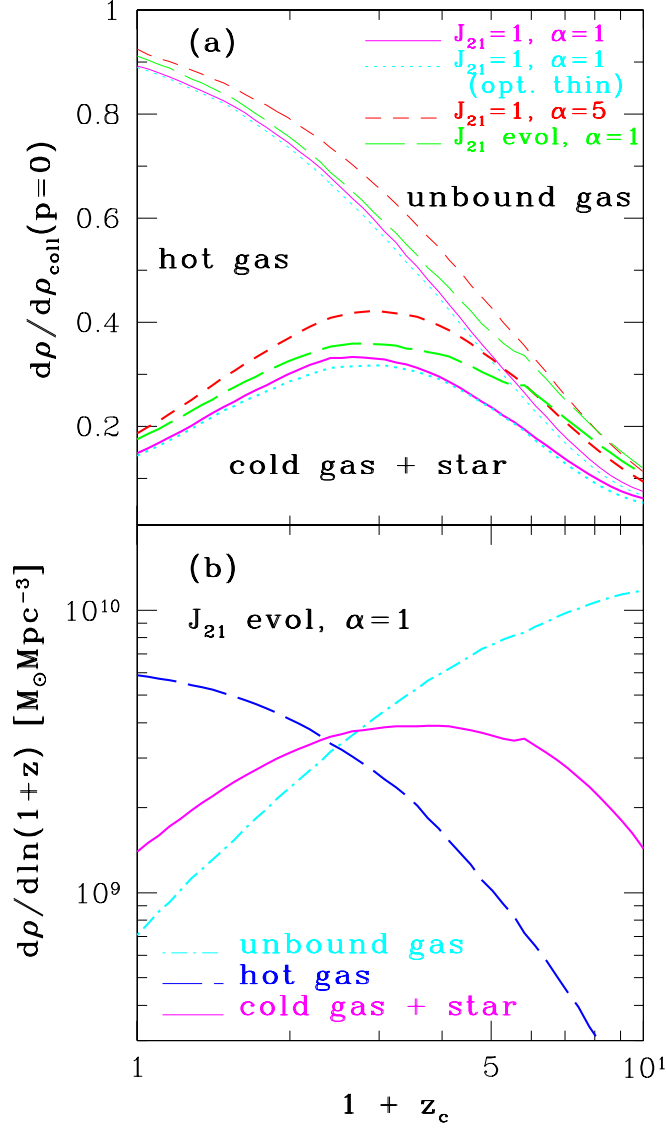


Fig. 13.— (a) The baryon density which cools (thick lines) or becomes bounded (thin lines) per Hubble time under the UV background, normalized by that which collapses in the absence of gas pressure. Lines specify different UV parameters as shown in the figure (unless indicated, absorption is considered). The three regions divided by thick and thin lines correspond to “cold gas + star”, “hot gas”, and “unbound gas”, respectively. (b) Production rates of “cold gas + star”, “hot gas”, and “unbound gas” for the evolving  $J_{21}$  and  $\alpha = 1$ . For both panels, the standard CDM model is assumed.

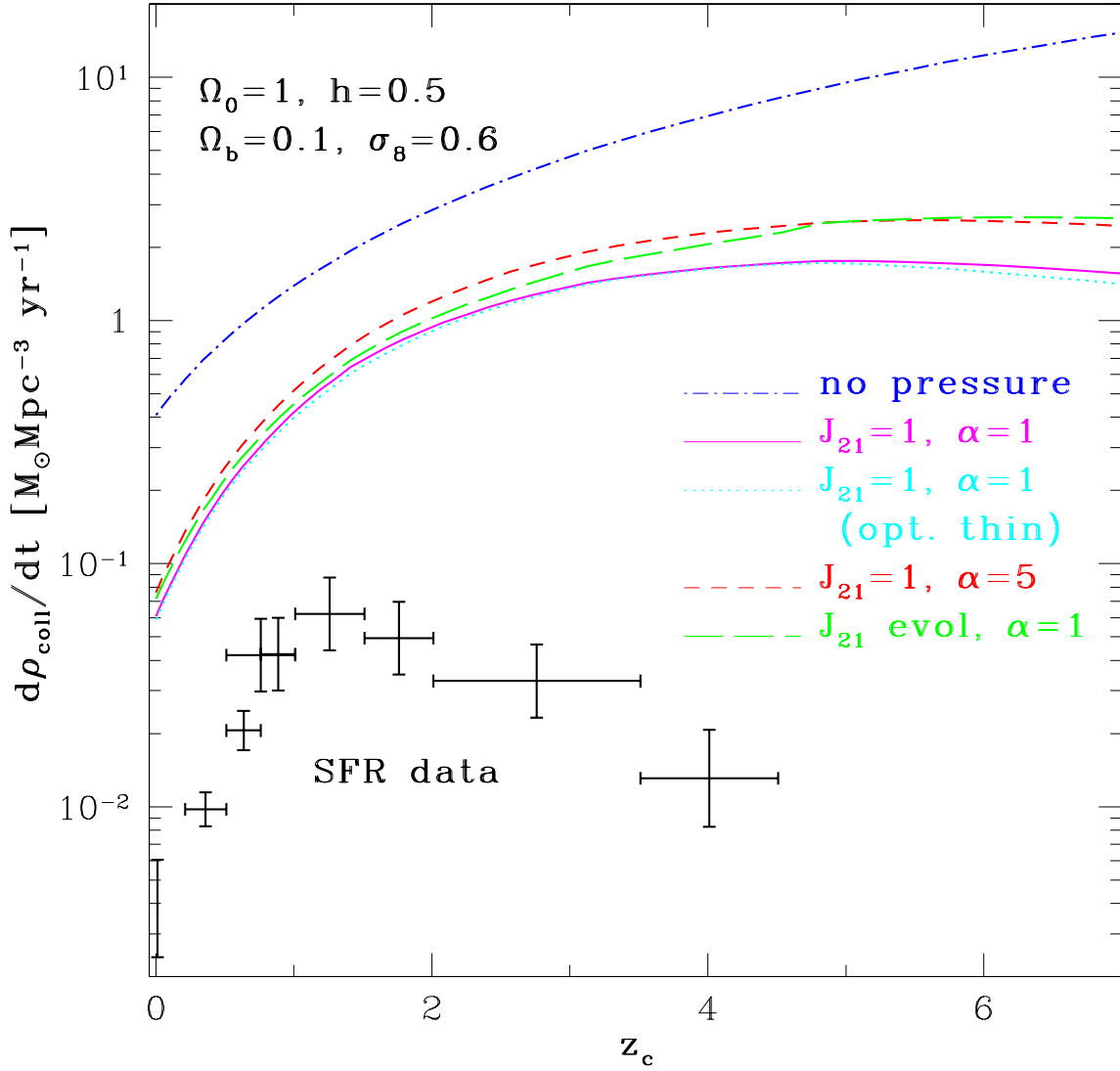


Fig. 14.— The global production rates of “cold gas + star” per year predicted in the standard CDM model (unless indicated, absorption is considered). Also potted for reference are the observed cosmic star formation rates (Madau et al. 1996, 1998; Lilly et al. 1996; Connolly et al. 1997), without corrections for the dust extinction, compiled by Totani et al. (1997) and Totani (1999, private communication).

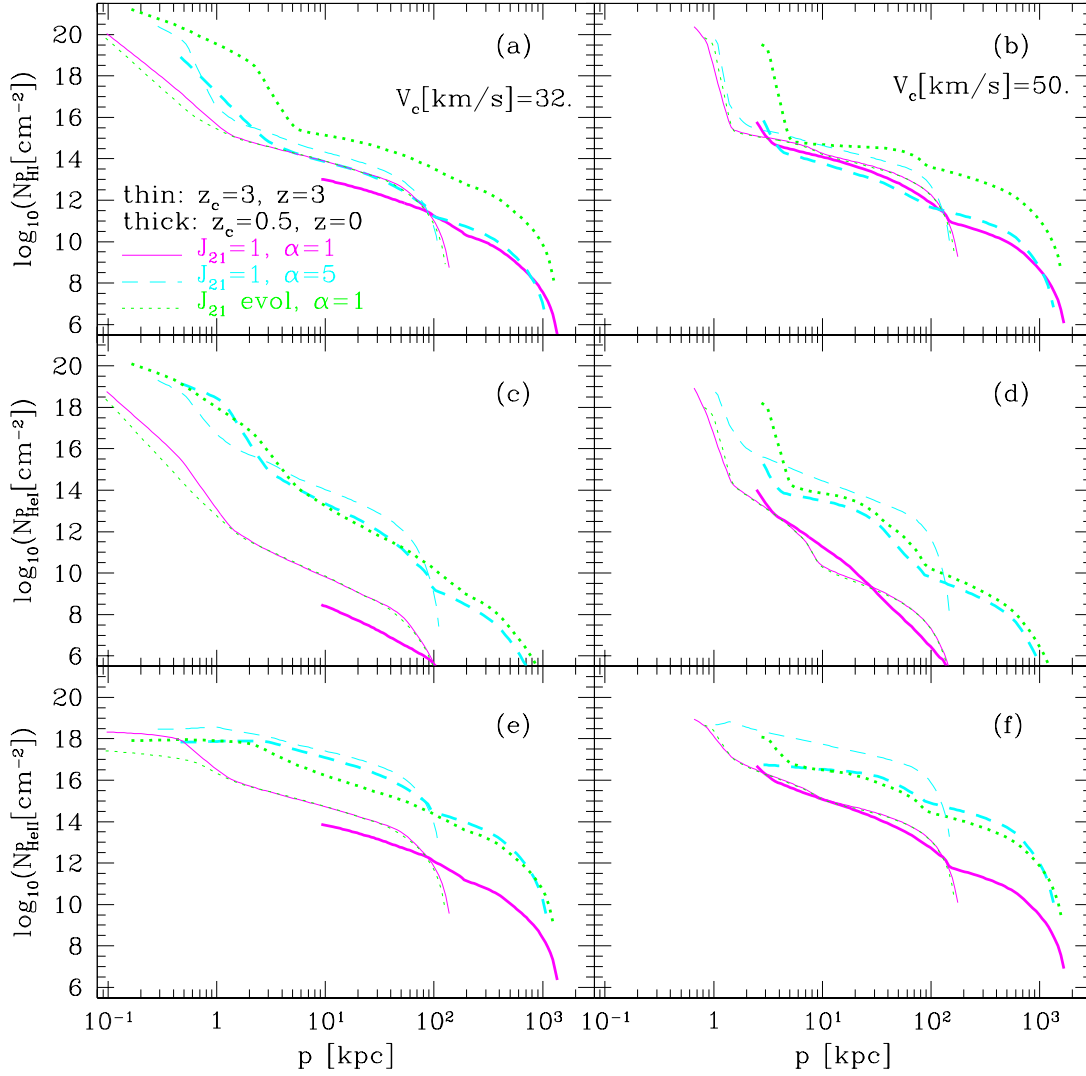


Fig. 15.— Line of sight column densities through the cloud  $N_j^P$  ( $j = \text{HI}, \text{HeI}, \text{HeII}$ ) as a function of impact parameter  $p$  for  $V_c = 32 \text{ km s}^{-1}$  (left panels) and  $V_c = 50 \text{ km s}^{-1}$  (right). Thick lines are the clouds with  $z_c = 3$  viewed at  $z = 3$ , while thin lines those with  $z_c = 0.5$  viewed at  $z = 0$ . Choices of the UV parameters (all with absorption) are as indicated in the figure.

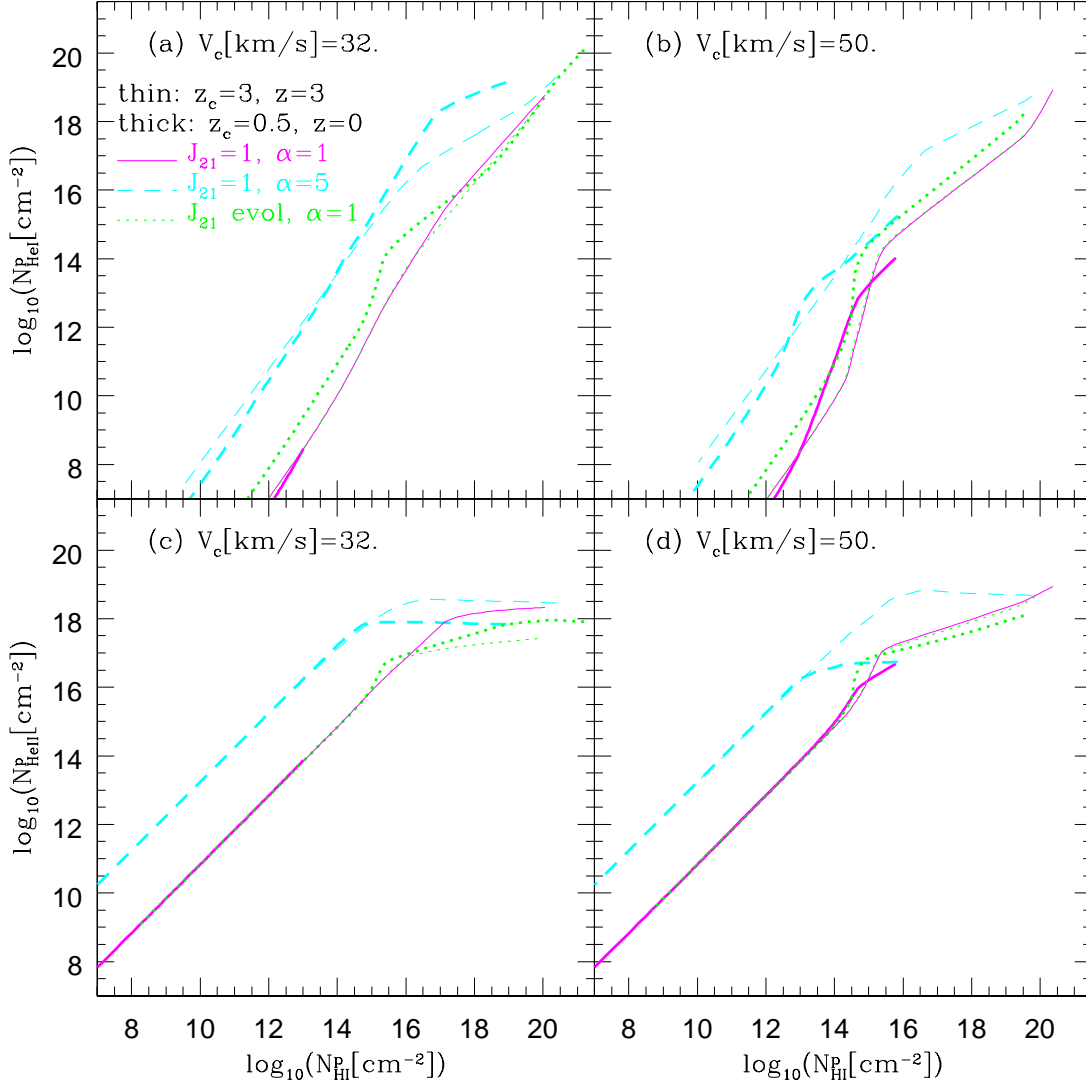


Fig. 16.— Same as Fig. 15, except that  $N_{\text{HeI}}^{\text{P}}$  (upper panels) and  $N_{\text{HeII}}^{\text{P}}$  (lower) are plotted against  $N_{\text{HI}}^{\text{P}}$ .

Table 1: Characteristic redshifts of simulation runs

	$z_i$	$z_{\text{ta}0}$	$z_{c0}$	$z_{\text{ta}}$	$z_c$
low-redshift collapse	40	5.4	3	1.3	0.5
middle-redshift collapse	110	16	10	5.4	3
high-redshift collapse	300	45	28	16	10

Table 2: The critical impact parameter  $p_{\text{crt}}$  (see text for definition) and the ratio of its square for the evolving  $J_{21}$  and  $\alpha = 1$

		$V_c = 32 \text{ km s}^{-1}$		$V_c = 50 \text{ km s}^{-1}$	
species		$p_{\text{crt}}$ [kpc]	ratio of $p_{\text{crt}}^2$	$p_{\text{crt}}$ [kpc]	ratio of $p_{\text{crt}}^2$
$z = 3$	HI	10	1	10	1
	HeI	0.8	1/156	1	1/100
	HeII	20	4	40	16
$z = 0$	HI	40	1	100	1
	HeI	10	1/16	10	1/100
	HeII	100	6.25	100	1

Table 3: Same as Table 2 except for  $J_{21} = 1$  and  $\alpha = 5$ .

		$V_c = 32 \text{ km s}^{-1}$		$V_c = 50 \text{ km s}^{-1}$	
species		$p_{\text{crt}}$ [kpc]	ratio of $p_{\text{crt}}^2$	$p_{\text{crt}}$ [kpc]	ratio of $p_{\text{crt}}^2$
$z = 3$	HI	20	1	30	1
	HeI	10	0.25	15	0.25
	HeII	100	25	150	25
$z = 0$	HI	10	1	10	1
	HeI	7	0.49	7	0.49
	HeII	200	400	400	1600

Table 4: Indices of column density distributions,  $N_j^p \propto p^{-n}$  and  $d\mathcal{N}/dN_j^p \propto (N_j^p)^{-\beta}$

species $j$	$V_c = 32 \text{ km s}^{-1}$		$V_c = 50 \text{ km s}^{-1}$	
	$n$	$\beta$	$n$	$\beta$
HI ( $N_{\text{HI}}^p < 10^{16} \text{ cm}^{-2}$ )	1.5	2.3	1.3	2.5
HI ( $N_{\text{HI}}^p > 10^{16} \text{ cm}^{-2}$ )	3	1.7	24	1.1
HeI	3.7	1.5	18	1.1
HeII	2	2	2.3	1.9

Table 5: Relations among  $N_{\text{HI}}^p$ ,  $N_{\text{HeI}}^p$  and  $N_{\text{HeII}}^p$  in cgs units

	$N_{\text{HI}}^p < 10^{16} \text{ cm}^{-2}$	$N_{\text{HI}}^p > 10^{16} \text{ cm}^{-2}$
$J_{21}$ evolving, $\alpha = 1$	$N_{\text{HeI}}^p \sim 10^{11} (N_{\text{HI}}^p / 10^{14})^{1.5}$ $N_{\text{HeII}}^p \sim 10 N_{\text{HI}}^p$	$N_{\text{HeI}}^p \sim 10^{-1} N_{\text{HI}}^p$ $N_{\text{HeII}}^p \sim 10^{18}$
$J_{21} = 1$ , $\alpha = 5$	$N_{\text{HeI}}^p \sim 10^{13} (N_{\text{HI}}^p / 10^{14})^{1.5}$ $N_{\text{HeII}}^p \sim 10^3 N_{\text{HI}}^p$	$N_{\text{HeI}}^p \sim 10 N_{\text{HI}}^p$ $N_{\text{HeII}}^p \sim 10^{18}$

Table 6: Photoionization cross section parameters in equation (A4)

species $i$	ionization energy $h\nu_i$ [eV]	amplitude $\sigma_i(\nu_i)$ [ $\text{cm}^2$ ]	index $\eta_i$
HI (1)	13.6	$6.30 \times 10^{-18}$	3.0
HeI (2)	24.6	$7.83 \times 10^{-18}$	2.05
HeII (3)	54.4	$1.58 \times 10^{-18}$	3.0